Icarus 219 (2012) 515–533

Contents lists available at SciVerse ScienceDirect

Icarus

journal homepage: www.elsevier.com/locate/icarus

N-body simulations of cohesion in dense planetary rings: A study of cohesion parameters

Randall P. Perrine, Derek C. Richardson *

Department of Astronomy, University of Maryland, College Park, MD 20740-2421, United States

ARTICLE INFO

Article history:
Received 31 July 2011
Revised 19 March 2012
Accepted 27 March 2012
Available online 5 April 2012

Keywords:
Planetary rings
Saturn, Rings
Tides, Solid body
Ices, Mechanical properties
Collisional physics

ABSTRACT

We present results from a large suite of simulations of Saturn's dense A and B rings using a new model of particle sticking in local simulations (Perrine, R.P., Richardson, D.C., Scheeres, D.J. [2011]. Icarus 212, 719–735). In this model, colliding particles can be incorporated into or help fragment rigid aggregations on the basis of certain user-specified parameters that can represent van der Waals forces or interlocking surface frost layers.

Our investigation is motivated by laboratory results that show that interpenetration of surface layers can allow impacting frost-covered ice spheres to stick together. In these experiments, cohesion only occurs below specific impact speeds, which happen to be characteristic of impact speeds in Saturn's rings. Our goal is to determine if weak bonding is consistent with ring observations, to constrain cohesion parameters in light of existing ring observations, to make predictions about particle populations throughout the rings, and to discover other diagnostics that may constrain bonding parameters.

We considered the effects of five parameters on the equilibrium characteristics of our ring simulations: speed-based merge and fragmentation limits, bond strength, ring surface density, and patch orbital distance (i.e., the A or B ring), some with both monodisperse and polydisperse comparison cases. In total, we present data from 95 simulations.

We find that weak cohesion is consistent with observations of the A and B rings (e.g., French, R.G., Nicholson, P.D. [2000]. Icarus 145, 502–523), and we present a range of simulation parameters that reproduce the observed size distribution and maximum particle size. It turns out that the parameters that match observations differ between the A and B rings, and we discuss the potential implications of this result. We also comment on other observable consequences of cohesion for the rings, such as optical depth and scale height effects, and discuss whether very large objects (e.g., "propeller" source objects) are grown bottom-up from cohesion of smaller ring particles.

1. Introduction

1.1. Motivation

As the small particles comprising the rings of Saturn are composed almost entirely of water ice (e.g., Cuzzi et al., 2009), many experimentalists have undertaken the task of measuring the coefficient of restitution (ϵ) in icy particle collisions (e.g., Bridges et al., 1984; Supulver et al., 1995). These experiments revealed that "clean" icy surfaces are quite elastic at low speeds (normal coefficient of restitution above 0.8 at $\sim$1 mm/s), but that a coating of water frost can reduce ϵ significantly (see Bridges et al. (2001) for a review). On the other hand, studies combining observations with simulations (e.g., Porco et al., 2008) have shown that impacts among ring particles in Saturn's rings must be fairly inelastic—implying that these particles are coated in an icy frost.

Interestingly, some of these experiments have revealed that frost-coated ice can stick at low impact speeds, forming a cohesive bond (Hatzes et al., 1991; Bridges et al., 1996, 2001; Supulver et al., 1997). In particular, Hatzes et al. (1991) describe this cohesion by invoking a "Velcro" model—the rough texture of the frost layers provide an interlocking structure for colliding particles. Particularly intriguing is their discovery of a critical impact speed for cohesion (hereafter called a "merge limit") of $\sim$0.3 mm/s (for 2.5 cm-radius bodies), as this speed is on the order of the gravitational escape speed (for a test particle on the surface) of an icy sphere 1 m in radius. If this cohesion mechanism is generic across size scales, and the particles in the dense rings of Saturn are experiencing cohesion, they may form large aggregations of material.

Analysis of recent observations of the rings of Saturn implies the need for such a bonding mechanism. Porco et al. (2008) show that the contrast in the azimuthal brightness asymmetry of Saturn's A

* Corresponding author. Fax: +1 301 314 9067.
E-mail address: dcr@astro.umd.edu (D.C. Richardson).

0019-1035/$ - see front matter © 2012 Elsevier Inc. All rights reserved.
http://dx.doi.org/10.1016/j.icarus.2012.03.032

ring (e.g., Salo et al., 2004; French et al., 2007; Porco et al., 2008) can be modeled using extremely dissipative particle interactions, such as would arise from bonding. As well, radial banded structures in Saturn's B ring elude explanation. Tremaine (2003) suggests that these zones occupy a region of dynamical phase-space that is "shear-free"—zones with zero Keplerian shear—and thus subject to a solid–liquid phase transition. These zones (~100 km in scale) may consist of large-scale transiently bonded particles that orbit Saturn as a solid.

1.1.1. Observational constraints on the particle size distribution in Saturn's A and B rings

Observations of the rings (Zebker et al. (1985) for Voyager 1 radio occultation experiments, French and Nicholson (2000) for the 1989 Earth-based observations of an occultation by the star 28 Sgr, and Cuzzi et al. (2009) for Cassini radio occultation observations) have revealed estimates of the size distribution and maximum particle size within different regions of the rings.

It should be noted that the results derived from these observations are model-dependent (i.e., "classical" vs. "thin layer"), and assume that the ring plane is composed of a loosely packed, uniformly distributed layer of particles (which is not likely to be true, considering the widely accepted presence of gravity wakes in dense rings—see Section 1.2). Also note that the Voyager results have greater fidelity than the Earth-based 28 Sgr occultation, and that results concerning the B ring carry greater uncertainty than those from the A ring, due to the difficulty of accurate measurements at such high optical depth. In this light, we only discuss these results in a broad overview, and apply them to constrain our data using a similarly broad target range (see Section 3.4).

Overall, the results of the modeling and data analysis from these three data sets are that the size distribution and maximum particle size in the A and B rings are roughly independent of the distance from Saturn. Adopting a functional form for the differential size distribution of $n(R) \propto R^{\alpha}$ (where $n(R)dR$ is the number of particles with radii between R and $R + dR$, and α is a parameter to be determined), they find α to be roughly between -2.5 and -3, and the maximum particle size[1] (R_{max}) to be 5–20 m (with the Voyager results favoring 5–10 m, and the stellar occultation showing a nearly constant 20 m). There may also be moderate trends with orbital distance from Saturn: each experiment showed a steepening of the size distribution from the inner to the outer A ring (α parameter from -2.7 to -3 for Voyager, and from -2.75 to -2.9 for the stellar occultations), and there are hints that R_{max} may increase with distance from Saturn (e.g., the Voyager experiment showed R_{max} increasing from 5 to 6 m in the inner and mid A ring to 9–11 m in the Encke gap region). We obtained these values from Table 15.1 of Cuzzi et al. (2009), and we refer the reader to that work for further details on these observations and how the signals were processed to obtain these numbers.

1.1.2. Numerical simulations of planetary rings

Studying the full effect of cohesive bonding in dense environments, specifically Saturn's dense A and B rings, requires detailed numerical modeling. Such systems involve a complex convergence of phenomena, including interparticle self-gravity, planetary tides, and interparticle collisions, and it may prove difficult to further incorporate dynamical bonding and fragmentation in a fully self-consistent way into current analytical models. Some groups have analytically modeled the effect of cohesion between a small number of bodies (e.g., Spahn et al., 2004; Albers and Spahn, 2006, using a viscoelastic model), and a few groups study planetary ring dynamics with local N-body simulations (e.g., Lewis and Stewart, 2000; Karjalainen and Salo, 2004; Porco et al., 2008), but none numerically model the emergent behavior of tens of thousands (or even millions) of N-body particles interacting with cohesion over many orbital times.

We created a new model that incorporates cohesion among N-body particles into a local, rotating frame (Perrine et al., 2011; hereafter Paper I). That work discusses the details of the model (including the considerations taken to combine a model of rigid aggregates with periodic boundary conditions), derivations of equations of motion for rigid aggregates in a rotating coordinate system, model tests, and initial results. Pertinent details of the method are summarized below in Section 1.3; for further discussion, see Paper I, or the doctoral dissertation by Perrine (2011).

We emphasize here that local simulations, first used in a planetary ring context (with linearized equations of motion to simplify computations; see Paper I) by Wisdom and Tremaine (1988), restrict the computational volume to a small region of interest (which we call a "patch"), enabling simulations with realistic surface densities and particle size distributions. For example, a full-ring simulation of Saturn's A and B rings with accurate surface densities and spherical 1-m-radius bodies would require roughly 10^{15} particles, which is far beyond current computational capability. But a representative patch may require only 10^5–10^9 bodies, depending on the specific problem being explored.

Also, regarding the cohesion model, we do not attempt to encapsulate all of the complex physics relevant to granular mechanics—rather the model represents a first step toward understanding how cohesion might affect particle dynamics in rings (see Paper I for further discussion).

The remainder of this paper is divided as follows. Section 1.2 defines a few select terms that we use in this paper, while Section 1.3 presents our model and its capabilities. Section 2 describes the simulations we performed, including a description and motivation for our range of cohesion and ring parameters. Section 3 first discusses the typical lifetime of an aggregate in our model, and then presents the results and implications of our simulations, addressing our key science goals. Lastly, Section 4 provides a summary with conclusions, and ideas for future work.

1.2. Terminology

In our model, cohesion leads to the formation of "aggregates" that are collections of particles joined via inflexible and incompressible bonds of user-defined strength. For example, this body can, depending on the strength of the bonds, resist self-gravitational reshaping (e.g., remain highly non-spherical). The constituents of an aggregate remain fixed with respect to one another as the aggregate moves and rotates in response to external forces and torques. Aggregates can agglomerate through collisional accretion with other bodies—free particles, or other aggregates—and can fragment through collisional events or stress fragmentation (when stresses exceed bond strengths).

Other researchers (e.g., Karjalainen and Salo, 2004; Karjalainen, 2007) use the term "aggregate" to refer to a collection of particles bound together by gravity alone. Following the terminology of Richardson et al. (2002), we refer to these structures as "gravitational aggregates." Unless indicated otherwise, "aggregate" in this paper refers to a bonded aggregate, though we use "bonded aggregate" at times for clarity. Both types of structures appear in our simulations (cf. Section 2, Figs. 1 and 2).

An important form of gravitational aggregate that is prevalent in dense ring simulations arises in the form of web-like structures usually referred to as "self-gravity wakes," which for simplicity we subsequently refer to as "wakes" (see Julian and Toomre (1966) and Salo (1992) for more detail, or Schmidt et al. (2009) for an

[1] Note that R_{max} may describe a single large body that, due to its low number frequency, does not necessarily lie on the overall size distribution. Its size could be well above the predicted cutoff.

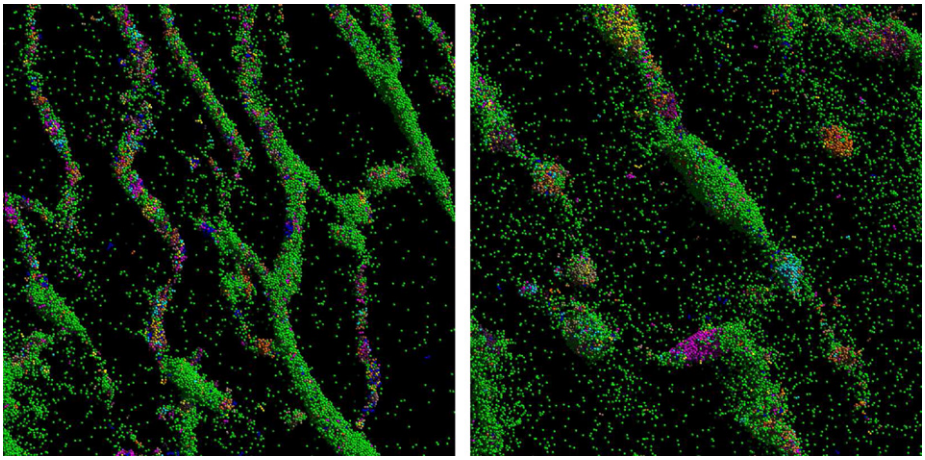

Fig. 1. Snapshots from A ring runs with moderate cohesion (A-F-mono-4, left; cf. Table 2) and high cohesion (A-M2-mono-9, right, cf. Table 1). For reference, the merge limit in the left pane is near the Hatzes et al. (1991) value, but the merge limit in the right pane is four times "stickier". The view of these local patches of ring material is face-on, with up as the orbital direction, and Saturn (not shown) located far to the left. These patches are approximately 350 m on a side as pictured, so this view only displays approximately half of the simulated region. To enhance aggregate visibility, particles bonded into aggregates (shown in non-green colors) are drawn overtop of non-bonded particles (in green)—thus, aggregates are never hidden behind a cluster of unbonded green particles. Conversely, clusters of green particles are unbonded gravitational aggregates; see for example the large object near-center on the right pane. Note the finer wake structure and abundance of small aggregates in the left pane, but coarser wake structure and larger embedded aggregates in the right pane. Strong bonding evidently not only enables larger aggregates, but begins to disrupt wake structure. (For interpretation of the references to color in this figure legend, the reader is referred to the web version of this article.)

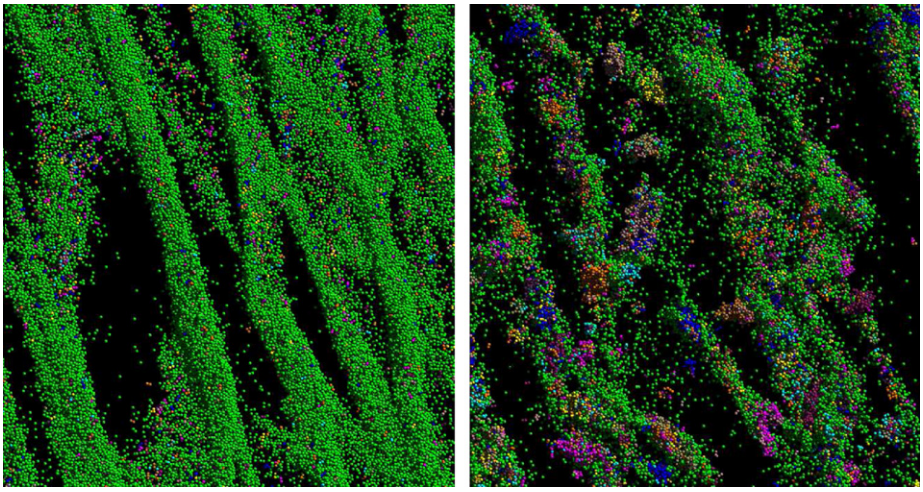

Fig. 2. Pictured here are two simulations based in the B ring using the same cohesion parameters as in Fig. 1, showing moderate cohesion (B-F-mono-4, left) and high cohesion (B-M2-mono-8, right). Viewing geometry and colors are as in Fig. 1. Note the drastic difference in structure between the two panes, in comparison to the two panes in Fig. 1—this demonstrates that there may be a relationship between the physical optical depth and cohesion parameters in the B ring, which is not present in the A ring (see Section 3.8). (For interpretation of the references to color in this figure legend, the reader is referred to the web version of this article.)

extended review). While these wakes have never been imaged directly (due to their currently unresolvable sub-hundred-meter size), they are predicted by many models (e.g., Salo, 1992; Richardson, 1994; Porco et al., 2008; Robbins et al., 2010). These structures are highly transient, forming and dissolving on orbital timescales, and form when the gravitational collapse due to particle self-gravity nearly balances the disruptive influence of Keplerian shear (i.e., when the Toomre Q parameter is near unity; Toomre, 1964). They take the form of elongated and densely packed gravitational aggregates, with a radial spacing estimated by λ_{crit}, the critical wavelength of the region,[2] and a characteristic pitch angle (orientation with respect to the orbital direction) of about 20–25°, depending on local conditions.

Important characteristic speed scales in our simulations include the particle escape speed (v_{esc}) and shear speed (v_{shear}). The former has the usual definition: the minimum initial speed for a massless test particle to reach infinity relative to an isolated ring particle, $v_{esc} = \sqrt{\frac{2Gm}{R}}$, where m and R are the mass and radius of the ring particle. For this definition, we ignore planetary gravity, tidal effects, and perturbations from other particles (or moons), as this quantity is merely used as a convenient normalization. The shear speed is the relative speed between two (massless) objects on circular orbits with semimajor axes separated by the sum of their radii, that just barely touch as the inner body overtakes the outer; in the linearized approximation (see Wisdom and Tremaine, 1988), $v_{shear} = \frac{3}{2}\Omega\delta a$, where δa is the difference in the particles' orbital semimajor axis—which is merely the sum of the particles' radii. The bodies are massless in this definition so that their

[2] The critical wavelength is the shortest axisymmetric wavelength stabilized by differential rotation alone: $\lambda_{crit} = 4\pi^2 G\Sigma/\Omega^2$, with G the gravitational constant, Σ the ring mass surface density, and Ω the orbital frequency of the comoving frame. See, for example, Salo (1992).

mutual gravitational attraction does not increase their relative speed.

We will use the escape and shear speeds to scale the impact speeds of particles in dense rings. In fact, these two quantities are nearly equal in the main rings of Saturn. For equal-size particles, their ratio depends only on the internal density of the particles and the orbital frequency, or $v_{esc}/v_{shear} \sim \sqrt{\rho}/\Omega$. (We apply this relationship to the results of our simulations in Section 3.5.)

Finally, in Paper I, we introduced a quantity β that defines the contact area assumed when discussing different bonding models, while at the same time encapsulating complex bonding physics into a simple term (similar to the concept of a coefficient of restitution). When any model calculates bond strength from relative acceleration or force, that model must specify the assumed contact area, as the contact area is the conversion factor between force and pressure. Thus, in this work, we quote the assumed β whenever a bond strength is discussed.

For the full derivation and discussion of β, we refer the reader to Appendices B and C in Paper I. In short, $\beta \equiv d/R$, or the ratio between the depth of particle surface layer interpenetration (d) to the radius of the equal-size bodies (R). More intuitively, at small values of β, β is approximately the ratio between the contact area and the particles' cross-section. (Note that for simplicity, we restrict ourselves here to the monodisperse case.)

For spheres that perfectly overlap, $\beta = 2$, and the resulting contact area is the cross-section of the particles: πR^2. Consequently, this is the largest possible β. While the image of such a particle configuration is quite unphysical, this is the most generic case. (Due to its generality, and ease of translation to other contact areas, the full particle cross-section is the contact area assumed in the model presented in Section 1.3—see below for examples.) The smallest possible β is 0, when there is no overlap, and thus the contact area is zero.

For clarity, in this work, we refer to simulation "parameter strengths" and "lab strengths." Parameter strengths refer to the modeled parameter used in the code, and lab strengths refer to an experimentally or observationally determined strength. The conversion between these two types of strengths is the β for the experiment; when $\beta \ll 1$, the relationship is:

$$(S_{Param}) = (\beta_{Lab})\ (S_{Lab}) \tag{1}$$

where S_{Param} and S_{Lab} are the parameter and lab strengths, respectively, and β_{Lab} is the conversion factor.

There are two means of calculating the β conversion factor between any experimental setup and our simulations: either combine d and R (e.g., for dynamic experiments involving spherical particles), or compute the ratio of the contact area to the cross-section of the simulated particles (e.g., static experiments using flat plates). For example, the bonding concept used in this work is based on overlapping frost layers; Hatzes et al. (1991) studied 2.5 cm ice spheres, and from their results we adopt the frost layer interpenetration to be $d \approx 25$ μm. With $R = 2.5$ cm, we have $\beta = 10^{-3}$. Using Eq. (1), a parameter strength of 100 Pa in the code would approximately match a lab strength of 10^5 Pa for the Hatzes et al. (1991) experiments. As another example, Supulver et al. (1997) used static plates in their apparatus (and thus R is undefined in this experiment). So we instead examine the ratio of their contact area ($\sim$1 cm^2) to the cross-section of a typical particle in our simulations ($\sim$1 m^2), which is $\beta \sim 10^{-4}$. So a lab strength in Supulver et al. (1997) of $\sim$100 Pa approximately matches a parameter strength of 10^{-2} Pa.

1.3. Numerical method

Our aggregation model is built into `pkdgrav`, an N-body code originally designed for cosmological simulations (Stadel, 2001), which was adapted to include particle collisions (Richardson et al., 2000) for the purpose of studying, among other things, planetary rings (e.g., Porco et al., 2008).

`Pkdgrav` uses a parallelized tree code to reduce the computational cost of summing up gravitational force contributions between particles (e.g., Barnes and Hut, 1986; Richardson, 1994). A second-order leapfrog scheme is used to integrate the equations of motion; collisions among particles are predicted and resolved during the drift phase by treating particle trajectories as linear and predicting when intersections occur.

The aggregation model works as follows. Colliding particles can stick on contact if the impact speed is below a user-defined threshold called the "merge limit." Fractal growth proceeds as more free particles—or other aggregates—collide and stick in this way.

Particles can fragment from an aggregate—becoming free, single particles—in two ways. First, a particle impacting an aggregate at a speed above another user-specified threshold (the "fragmentation limit") causes the impacted particle to become liberated from the aggregate. If the impacting particle is itself part of an aggregate, it may be liberated as well. Liberated particles will likely immediately strike other particles in their respective former aggregates, which might also become liberated (if the impact speeds are still high enough), causing a fragmentation cascade.

Second, each aggregate is assigned a user-defined strength in the normal (tensile) or tangential (shear) directions. Any particle whose acceleration relative to its aggregate's center of mass exceeds the stress limit is liberated from the aggregate and becomes a free particle again at its current position and velocity. The aggregate experiences no strain as the stress increases: it remains perfectly rigid until the strength is exceeded.

For these calculations, the parameter strength, in units of pressure, is converted to a maximum acceleration by multiplying by the cross-sectional area of the particles and dividing by the mass of the particle under consideration. This choice is made in order to remain a general and simple method to explore the effects of cohesion, no matter the means of sticking under study. If desired, the user of the code may translate the parameter strength used within `pkdgrav` into the appropriate lab strength for the desired bonding method. This is achieved by scaling the parameter strength by the ratio of the cross-sectional area to the true contact area by the experiment's β parameter (see Section 1.2).

The reader should keep in mind that this cohesion model is quite general, and it is only an approximation to the behavior of real cohesive materials. For instance, in our model, particles have no knowledge of which particle(s) they are stuck to—all a particle "knows" is which aggregate it belongs to. Aggregate properties are calculated based on the positions, velocities, spins, etc., of the particles included in that body alone. Our simple tool is not capable of modeling sophisticated granular and solid-body physics, such as a force network (e.g., Lois and Carlson, 2007), as that level of detail is beyond the scope of this work. For more detail, see the doctoral dissertation by Perrine (2011).

2. Simulations

2.1. Parameters

The simulations presented here generally employed the same parameters as in Paper I. Settings consistent across all simulations will be discussed first.

The internal density for all particles was 0.5 g/cm^3, representing porous ice. This is consistent with the local Roche critical density (the density of material that would fill its own Roche lobe, $\rho_R \sim 1.88 M_S/a^3$, with M_S the mass of Saturn and a the patch semi-major axis; see for example Tiscareno et al., 2008) for the A ring

(Porco et al., 2007). For simplicity, we used the same internal density for all A and B ring simulations, even though the local Roche density should be higher for the B ring region (see Section 3.6 for more discussion).

Following Porco et al. (2008), we used the speed-dependent normal coefficient of restitution (ϵ) law from Borderies et al. (1984), with an extremely dissipative v^* of 0.001 cm/s, with zero surface friction. This choice of v^* means all impacts with speeds above 2 mm/s use an ϵ below 0.1, and the typical impact speed of 0.5 mm/s (the escape speed from a particle with the above parameters) has an ϵ of approximately 0.2—which appears consistent with the dissipative nature of frost-covered ice (e.g., Bridges et al., 2001).

The gravity tree's critical opening angle (θ_{crit}) was 0.5 radian (see Richardson, 1994 for more discussion), and the timestep was approximately 5 s. Each of these parameters were refined with convergence tests to optimize computational expediency and accuracy.

The dimensions of our patches were constant within the A or B ring simulations: approximately 880 by 350 m for the A ring, and 695 by 280 m for the B ring, with the longer axis in the azimuthal direction (the aspect ratio of 2:5 was chosen to accommodate the pitch angle of the gravity wakes). For our fiducial choices of surface mass density (Σ) for each ring (500 and 1000 kg/m^2 for the A and B ring, respectively), these correspond to 4 by 10 critical wavelengths (λ_{crit}—see Section 1.2).

But changing Σ can change N; for simplicity, and to keep N tractable (as runtime scales—at best—with N^2, due to geometrically increasing collision frequency), we chose to keep our patch size static when varying Σ (rather than forcing larger patches with increases in λ_{crit}). This means that at higher surface densities (and thus larger λ_{crit}'s) we are at higher risk for self-interaction among the wakes (between the simulated patch and its replicated ghost cells). However, our densest patches are at worst double the Σ of our fiducial—and were thus 2 by 5λ_{crit}—and our experience is that 2 by 5λ_{crit} provides reliably similar results to the fiducial patch size, so we feel that this is an acceptable compromise between numerical accuracy and runtime.

We placed our simulated patches at two orbital semimajor axes to mimic B and A ring conditions, at 100,000 and 136,530 km from Saturn, respectively (with orbital periods of 8.96 and 14.3 h). The majority of our simulations used a 1-m-radius monodisperse particle population (again, the choice to use relatively large particles is to keep N tractable). For comparison purposes, some simulations were performed with polydisperse particles, with a size range of 0.8–1.2 m, and using a power-law size distribution exponent $\alpha = -3$, assuming the form $n(R) \propto R^{\alpha}$. These choices result in very similar N between the polydisperse and the monodisperse cases. (Note that the average particle radius in the polydisperse case is approximately 0.96 m, which means that v_{esc} will be ~4% smaller on average in the polydisperse cases than in the monodisperse.) In either case, a size distribution of aggregates emerges as the simulations proceed, resulting in changes to the overall effective α.

Given our choice of particle size, fiducial Σ, and patch size, the number of particles, N, was about 75,000 in the majority of our runs. As discussed, runs with larger Σ values had more particles, as N scales linearly with Σ (at constant patch area).

Our initial conditions were also identical to the setup presented in Paper I: each particle began as a free, non-spinning particle, with a random position and velocity. Each run was carried out for a similar time as in Paper I: usually to about nine simulated days (15 orbits for our A ring runs, 24 orbits for the B ring runs). This gives plenty of time for studying the equilibrium state of the system, as equilibrium is established within approximately five orbits (as determined when properties such as velocity dispersion and optical depth level off).

Most of our simulations completed in 8–11 days on 16 processors (cores), depending on the interparticle collision rate—but the highest Σ runs took drastically longer. In fact, our B ring simulation with the highest Σ (2000 kg/m^2) required 130,000 CPU hours (nearly 15 CPU years) of computation.

Our simulations explored the parameter space by holding certain values constant while varying a single parameter, in order to isolate the effects of that parameter. Different suites of simulations explored the effects of the merge and fragmentation limits, bond strength, and mass surface density (see Tables 1–3). When available, we chose best-guess fiducial values and reasonable ranges for our parameters based on observational, experimental, or theoretical considerations.

Our fiducial merge limit was 0.27 mm/s, or 0.5v_{esc} for R = 1 m, which remains a constant numerical value for every body throughout a simulation (rather than scaling by local properties, such as aggregate size). This value was based on the results of Hatzes et al. (1991), who found the critical sticking speed for frosty 2.5 cm ice spheres to be ~0.3 mm/s. We recognize that there likely is a relationship between merge limit and radius (considering varying surface curvature and gravity scaling with particle size), but we are constrained to larger particle sizes (see above) for which no cohesion data yet exists.

We have no firm experimental reference for the impact fragmentation limit, but results from Bridges et al. (1996) indicate that this quantity may be on the order of 1 mm/s. Fig. 2a in Bridges et al. (1996) shows an impacting particle's speed decreasing as it rebounds, showing that the particles formed a cohesive bond during the impact that then broke, losing energy to the failing bond. That is, the impactor broke its own bond as it moved away faster than the bond could hold, and thus the impact speed (1.5 mm/s) exceeded the impact fragmentation limit for these particles.

Thus for the fiducial fragmentation limit, we chose two physically reasonable values of 0.53 and 1.06 mm/s (i.e., 1 and 2v_{esc} for

Table 1
First in a series of tables of simulation parameters, with each row representing a simulation. The first column is the simulation index, as explained in Section 2.1. The next 3 columns are the bonding parameters: merge limit (M), fragmentation limit (F), and strength (S), in either units of v_{esc} (0.53 mm/s; the escape speed from a spherical particle with radius of 1 m and density 0.5 g/cm^3), or Pascals. The last column is the mass surface density (Σ). The total combined CPU time for all the runs represented on these tables is over 561,000 CPU hours.

Index	M (v_{esc})	F (v_{esc})	S (Pa)	Σ (kg/m^2)
A-M1-mono-1	0.01	1.0	10^2	500
A-M1-mono-2	0.05	–	–	–
A-M1-mono-3	0.1	–	–	–
A-M1-mono-4	0.175	–	–	–
A-M1-mono-5	0.25	–	–	–
A-M1-mono-6	0.375	–	–	–
A-M1-mono-7	0.5	–	–	–
A-M1-mono-8	0.75	–	–	–
A-M1-mono-9	1.0	–	–	–
A-M1-poly-1	0.01	1.0	10^2	500
A-M1-poly-2	0.05	–	–	–
A-M1-poly-3	0.1	–	–	–
A-M1-poly-4	0.175	–	–	–
A-M1-poly-5	0.25	–	–	–
A-M1-poly-6	0.5	–	–	–
A-M1-poly-7	1.0	–	–	–
A-M2-mono-1	0.05	2.0	10^2	500
A-M2-mono-2	0.25	–	–	–
A-M2-mono-3	0.5	–	–	–
A-M2-mono-4	0.75	–	–	–
A-M2-mono-5	1	–	–	–
A-M2-mono-6	1.25	–	–	–
A-M2-mono-7	1.5	–	–	–
A-M2-mono-8	1.75	–	–	–
A-M2-mono-9	2.0	–	–	–

Table 2
Second in a series of tables of simulation parameters; this table continues to detail the A ring runs. See Table 1 for details.

Index	M (v_{esc})	F (v_{esc})	S (Pa)	Σ (kg/m^2)
A-F-mono-1	0.5	0.5	10^2	500
A-F-mono-2	–	0.75	–	–
A-F-mono-3	–	1.0	–	–
A-F-mono-4	–	1.25	–	–
A-F-mono-5	–	1.5	–	–
A-F-mono-6	–	1.75	–	–
A-F-mono-7	–	2.0	–	–
A-F-mono-8	–	2.5	–	–
A-F-mono-9	–	3.0	–	–
A-F-mono-10	–	3.5	–	–
A-F-mono-11	–	4.0	–	–
A-F-poly-1	0.5	0.5	10^2	500
A-F-poly-2	–	0.75	–	–
A-F-poly-3	–	1.0	–	–
A-F-poly-4	–	1.25	–	–
A-F-poly-5	–	1.5	–	–
A-F-poly-6	–	1.75	–	–
A-F-poly-7	–	2.0	–	–
A-F-poly-8	–	2.5	–	–
A-F-poly-9	–	3.0	–	–
A-Str-mono-1	0.5	1.0	10^{-5}	500
A-Str-mono-2	–	–	10^{-4}	–
A-Str-mono-3	–	–	10^{-3}	–
A-Str-mono-4	–	–	10^{-2}	–
A-Str-mono-5	–	–	10^{-1}	–
A-Str-mono-6	–	–	10^{0}	–
A-Str-mono-7	–	–	10^{1}	–
A-Str-mono-8	–	–	10^{2}	–
A-Str-mono-9	–	–	Infinite	–
A-Sig-mono-1	0.5	1.0	10^2	125
A-Sig-mono-2	–	–	–	250
A-Sig-mono-3	–	–	–	375
A-Sig-mono-4	–	–	–	437
A-Sig-mono-5	–	–	–	500
A-Sig-mono-6	–	–	–	625
A-Sig-mono-7	–	–	–	750
A-Sig-mono-8	–	–	–	1000

Table 3
Third in a series of tables of simulation parameters; this table details all of the B ring runs. See Table 1 for details. (Note that B-Sig-mono-7 is included here, even though it remains incomplete.)

Index	M (v_{esc})	F (v_{esc})	S (Pa)	Σ (kg/m^2)
B-M1-mono-1	0.0	1.0	10^2	1000
B-M1-mono-2	0.01	–	–	–
B-M1-mono-3	0.05	–	–	–
B-M1-mono-4	0.1	–	–	–
B-M1-mono-5	0.25	–	–	–
B-M1-mono-6	0.5	–	–	–
B-M1-mono-7	0.75	–	–	–
B-M1-mono-8	1.0	–	–	–
B-M2-mono-1	0.05	2.0	10^2	1000
B-M2-mono-2	0.1	–	–	–
B-M2-mono-3	0.25	–	–	–
B-M2-mono-4	0.5	–	–	–
B-M2-mono-5	0.75	–	–	–
B-M2-mono-6	1.0	–	–	–
B-M2-mono-7	1.5	–	–	–
B-M2-mono-8	2.0	–	–	–
B-F-mono-1	0.5	0.5	10^2	1000
B-F-mono-2	–	0.75	–	–
B-F-mono-3	–	1.0	–	–
B-F-mono-4	–	1.25	–	–
B-F-mono-5	–	1.5	–	–
B-F-mono-6	–	1.75	–	–
B-F-mono-7	–	2.0	–	–
B-F-mono-8	–	2.5	–	–
B-F-mono-9	–	3.0	–	–
B-Str-mono-1	0.5	1.0	10^{-5}	1000
B-Str-mono-2	–	–	10^{-4}	–
B-Str-mono-3	–	–	10^{-3}	–
B-Str-mono-4	–	–	10^{-2}	–
B-Str-mono-5	–	–	10^{-1}	–
B-Str-mono-6	–	–	10^{0}	–
B-Str-mono-7	–	–	10^{1}	–
B-Str-mono-8	–	–	10^{2}	–
B-Sig-mono-1	0.5	1.0	10^2	250
B-Sig-mono-2	–	–	–	500
B-Sig-mono-3	–	–	–	750
B-Sig-mono-4	–	–	–	1000
B-Sig-mono-5	–	–	–	1250
B-Sig-mono-6	–	–	–	1500
B-Sig-mono-7	–	–	–	2000

our porous icy $R = 1$ m spheres). In our model, the fragmentation limit cannot be lower than the merge limit, so to choose a lower fiducial fragmentation limit would further confine the merge limit range during parameter sweeps. Thus the lower limit of $1\,v_{esc}$ is perhaps more physically grounded, but the larger limit of $2\,v_{esc}$ allows us to explore higher merge limits, and both are consistent with the observation from Bridges et al. (1996). (Again, curvature and gravity scaling may alter the fragmentation limit for our larger particles, but we use these fiducials in the absence of further data.)

We used 100 Pa as our fiducial bond strength. This appears consistent with the measured strengths of the only extraterrestrial Solar System ice whose strength has been studied: comets. First, 100 Pa appears consistent with the analysis by Sekanina and Yeomans (1985) for the strength of Comet Brooks 2. Yet Asphaug and Benz (1996) found a weaker upper limit (~5 Pa) for the strength of Comet Shoemaker–Levy 9, while Richardson et al. (2007) found a higher upper limit of $\sim 10^3$–10^4 for Temple 1 (though the results are consistent with zero strength). This fiducial appears to be a reasonable midpoint.

However, comets are compositionally and structurally different from the particles comprising the rings of Saturn (as they include, for example, dust, methane, and organics—see for example Sitko et al., 2011), so their strengths are used here only as a starting reference. For comparison, the experiments of Supulver et al. (1997) showed frosty ice bonds failing with forces on the order of ~1000 dynes. At a contact area of ~1 cm^2, that is approximately a bond strength of 1000 dyn/cm^2, or 100 Pa. Again, this value is only a fiducial, as the experiments showed that this bond strength is variable based on the frost thickness and density (Supulver et al., 1997) and impact speed (Bridges et al., 1996).

Keeping in mind the discussion of parameter vs. lab strength from Section 1.2, our fiducial *parameter* strength of 100 Pa could translate into a lab strength that is higher than the upper limits found observationally for comets, as well as the experimental results for frosty ice cohesion (Supulver et al., 1997). However, this value is only a fiducial, and we have conducted a strength-varying suite in order to test the population's sensitivity to strength. (See Section 3.3 for a discussion of our results regarding the strength parameter.)

While our fiducial fragmentation limits and strength seem plausible, we believe that they are also roughly consistent with one another. Included in Paper I is a rough order-of-magnitude estimate relating the impact speed between two bodies (v_{imp}) and the pressure exerted by that impact (P_{imp}):

$$\left(\frac{1}{\beta}\right)\left(\frac{R}{1\text{ m}}\right)\left(\frac{\rho}{1\text{ g/cm}^3}\right)\left(\frac{v_{imp}}{1\text{ mm/s}}\right)\left(\frac{1\text{ s}}{\Delta t}\right) = \left(\frac{P_{imp}}{1\text{ Pa}}\right) \tag{2}$$

with R the radius of the (equal-size) impacting bodies, ρ the internal mass density of the bodies, Δt the timescale of the collision, and assuming $\beta \ll 1$. This relationship allows us to understand how the impact fragmentation limit (a speed) should scale with the bond strength (a pressure), while enabling a convenient scaling between these two failure limits.

Assuming $R = 1$ m, $\rho = 0.5$ g/cm^3, and $\Delta t = 0.01$ s (see Paper I), we find that an impact fragmentation limit of 0.5 mm/s is approximately consistent with an aggregate parameter strength (i.e., $\beta = 2$) of 25 Pa (or a lab strength of 10^5 Pa, using $\beta_{Lab} = 10^{-3}$). Thus a fragmentation limit of 0.5 mm/s is within an order of magnitude of our fiducial parameter strength (100 Pa).

Our fiducial Σ values for the A and B ring were 500 kg/m^2 for the A ring and 1000 kg/m^2 for the B ring, producing approximately equal computational load for each location within the rings. At $R = 1$ m, the geometric optical depths (i.e., total particle cross-sectional area divided by the area of the patch) are 0.75 and 1.5 for our A and B ring models, respectively.

Our A ring Σ value is based on the consistent results found both by Colwell et al. (2009; a compilation of density wave observations[3]) and Robbins et al. (2010; *N*-body work that matched simulated optical depth as a function of surface density to Cassini UVIS stellar occultation data). The true B ring Σ may be much larger than 1000 kg/m^2 (Robbins et al., 2010), but even doubling to 2000 kg/m^2 turned out to be extraordinarily expensive (as mentioned above, our 2000 kg/m^2 simulation required nearly 15 CPU years to complete). Thus we maintained the B ring fiducial of 1000 kg/m^2 in the interest of completing a large number of simulations to produce parameter sweeps—being sure to also provide a suite studying the aggregates' state at a range of Σ's.

For details regarding the remaining parameters, see Tables 1–3, in which runs are organized into suites with one changing parameter and all others constant (as indicated by dashes). The tables state an "Index" for each run, which is a shorthand for the parameters of interest in that simulation. The first term is A or B, indicating A or B ring nominal parameters (saturnian distance and surface density). The second term indicates the parameter varied in that suite, with *M* for merge limit, *F* for fragmentation limit, Str for strength, and Sig for surface density; when the merge limit is varied, we specify the fragmentation limit used (1 or 2 v_{esc}), as we employ two different fragmentation limits in such runs. The third term is the nature of the innate particle population, either monodisperse ("mono"—all particles having radius of 1 m) or polydisperse ("poly"—radii of 0.8–1.2 m, with $\alpha = -3$). Finally, the fourth term is a convenient run index within the suite. When we reference a suite throughout this paper, we simply state the three first terms of the indices of the runs in that suite; for example, the first suite in Table 1 is A-M1-mono (i.e., nominal A ring settings, with variable merge limit, fixing the fragmentation limit to 1 v_{esc}, and monodisperse initial particles).

Note that some parameters are duplicated across different runs; to save computation, we often used a single run in many suites (e.g., entries A-M1-mono-7, A-F-mono-3, and A-Sig-mono-5 are the same simulation). However, we did occasionally take the opportunity to rerun a simulation (with the same parameters and initial conditions) in order to verify that repeating a simulation reproduces consistent results (e.g., entries B-M2-mono-4 and B-F-mono-7 are independent simulations with the same parameters). Additionally, this afforded us the opportunity to confirm that we were getting uniform results between the two different computer systems we used for our runs.

2.2. Data analysis

The majority of the data analysis proceeded as described in Paper I; we present a summary of our procedures here, and outline an important change to our calculation for α below.

[3] Surface density is obtained directly from the density wave's wavelength dispersion as the wave propagates through the ring material; see Tiscareno et al. (2007) for a discussion of the technique.

Once the particles equilibrate (as determined by examining dynamical properties such as filling factor at the midplane and velocity dispersion), a simulation proceeds for approximately 10 orbits, during which we sample the state of the system ~10 times per orbit—measuring, for example, the percentage of free (unbonded) particles, the number of aggregates (including 2-particle "dumbbells"), the radius of the largest aggregate (R_{max}), the slope of the size distribution (α), the physical optical depth (τ_{phys}), and the particle vertical scale height (h).

We estimate the effective radius of our highly non-spherical aggregates by finding the radius of the volume-equivalent sphere (see Paper I). Once the sizes of the aggregates are known, we bin the data into a log–log histogram, and measure the slope of the line (see Fig. 3). In contrast to Paper I's method, we remove from the slope all bins with bodies less than 1.2 m in radius; we found that the results from the monodisperse and polydisperse runs showed improved agreement when we used this method, as it essentially ignores all unbonded bodies in both types of simulations. For example, Fig. 3 shows that particles in the first bin are far overrepresented in the power law, and would drastically skew the fit if included. Moreover, in the polydisperse case, there is more than one overrepresented bin, as there are unbonded bodies of many sizes in those plots—thus the polydisperse and monodisperse cases would include *different* biases if these bins were included. So our convention now is to ignore bins that include unbonded particles, or $R \leqslant 1.2$ m. It is possible that these unbonded particles are overrepresented because of their artificial indestructibility—these particles would perhaps in reality break down into a distribution of ever-smaller particles, which may in equilibrium match with the rest of the aggregate population. But this is beyond the scope of the model at this time.

Two example density distribution plots (from the same snapshots as in Fig. 3) are shown in Fig. 4. Note that Figs. 3 and 4 show similar trends and features, strongly indicating that larger bodies have consistently lower density than their constituent particles. This is not surprising; if the fractal dimension of our aggregates is under 3 (see Richardson, 1995 for a discussion), a random (inefficient) packing of spheres should leave more and more empty space between the objects as more spheres are added, resulting in an overall drop in density as the body grows.

The physical optical depth (τ_{phys}) is determined by firing "test rays" into the particle field at random locations normal to the plane of the ring, and computing the probability that the rays pass through the ring. Specifically, $e^{-\tau_{phys}} \equiv n/N$, where n is the number of test rays that pass through the ring and N is the total number of rays fired. Thus τ_{phys} is infinite if $n = 0$ (fully opaque), and $\tau_{phys} = 0$ if $n = N$ (fully transparent). The final quantity derived from the simulations, h, is the RMS vertical height of all of the particle centers in the patch.

Once each quantity is determined for each sampled timestep, we take the average and standard deviation of these quantities over time. This is necessary to remove the natural variability of all of these quantities even when the system is in equilibrium; see Paper I, Fig. 6, for an example. Scatter in τ_{phys} and h can be attributed to formation and destruction of wakes, and similar scatter in the aggregate properties is caused by stochastic bursts of aggregate formation. These processes are related, as aggregates tend to form readily as wakes collide, creating zones of low encounter speeds and high densities, as discussed in Section 3.1 and Paper I.

Note that this averaging procedure may help our results more closely match observations. While our simulations study a small patch of ring material for a long temporal baseline (approximately a week), observations typically image a large portion of ring material all at once, studying a large spatial baseline at one instant. These two techniques should yield similar results, as each

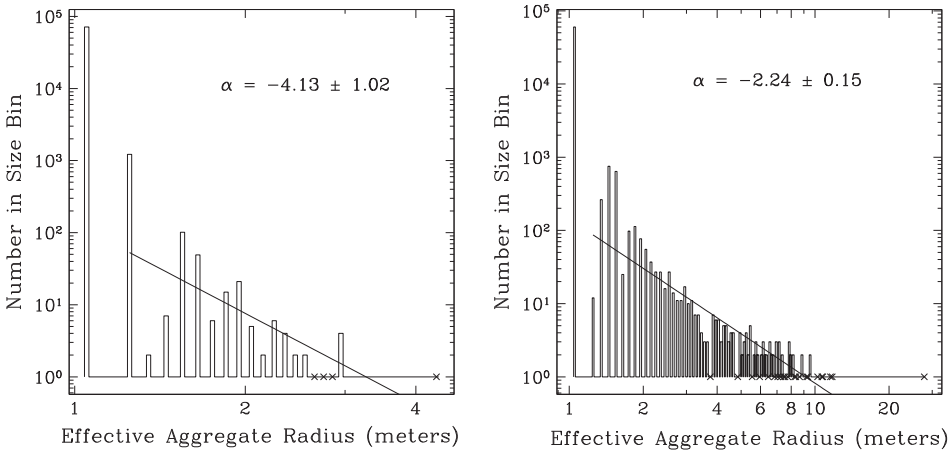

Fig. 3. Two example incremental size distributions of effective radii of bodies, chosen from snapshots of two simulations. The left pane shows the final state of the aggregate population in run A-M2-mono-1, demonstrating the relatively steep size distribution (and smaller number of aggregates) that comes with weaker cohesion. The right pane shows the final state of the aggregate population in a run with stronger cohesion, A-F-mono-5, in which larger bodies flatten out the size distribution. Plotting conventions are as in Paper I: bins are 0.1 m wide, ×'s indicate bins that contain exactly one body, and the result of the least-squares fit to the histogram's slope on this log–log plot is given as α (with $1-\sigma$ uncertainty). Note that in each plot there is a gap between the largest body and the next-largest body (and the location where the slope intercepts the x-axis). In this work, when we discuss the largest aggregate (R_{max}), we refer to the single body to the far right of these plots. (If we were to instead define R_{max} as the x-intercept, for example, our results for R_{max} would decrease by a significant amount, ∼33–50%, so this is an important distinction.) Also note that the fit does not include bodies of radius less than 1.2 m (a change from Paper I).

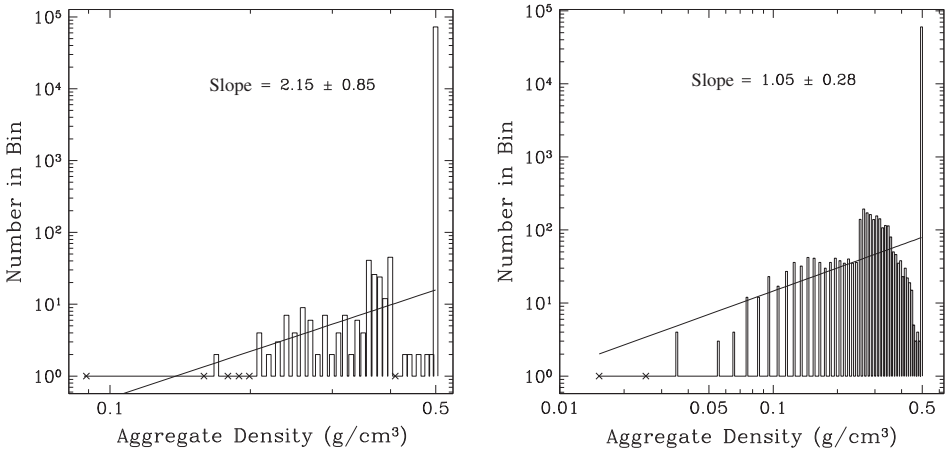

Fig. 4. Two example aggregate density distributions, chosen from the same snapshots as Fig. 3 (i.e., run A-M2-mono-1, using weaker cohesion, left, and run A-F-mono-5, with stronger cohesion, right). Density is computed as $(3M)/(4\pi R^3)$, with M the mass of the aggregate (sum of the masses of its constituent particles), and R the aggregate's effective radius (as defined in the text). Bins are 0.01 g/cm^3 wide, and—as in Fig. 3—×'s indicate bins that contain exactly one body, and the result of the least-squares fit to the histogram's slope on this log–log plot is given (with $1-\sigma$ uncertainty). Note that these figures approximately mirror those of Fig. 3, with all of the unaggregated bodies falling in the rightmost bin at 0.5 g/cm^3, and the rarer large aggregates having the lowest densities. (The fit given here is merely for demonstration purposes, so it includes the unaggregated bodies—in contrast to Fig. 3.)

technique removes natural variability by averaging and estimating error from internal variability in the sample.

Note that our calculation of the size distribution of bodies in our simulations only includes bonded aggregates, and that any loosely bound gravitational aggregates (such as wakes) do not affect our determination of α. This may be in contrast to what observers have measured, as those observations are based on light interacting with the rings in total, which cannot distinguish between gravitational and bonded aggregates as easily. We have not attempted to include gravitational aggregates into our data analysis; this is an area of future work.

3. Results and discussion

The results of our simulations (whose parameters are detailed in Tables 1–3), analyzed as discussed in Section 2.2, are plotted in Figs. 5–11. See the captions for further details.

3.1. The lifetime of a typical aggregate

Here we provide a brief description of the growth and destruction of a typical bonded aggregate. As discussed in Section 2.2, aggregates form chiefly in the high-density and low-relative-speed environment of the gravitational wakes. Then, as mentioned in Section 1.2, the wakes are short-lived, and dissolve on orbital timescales, due to the shearing nature of the disk. The dissolved wakes leave behind newly created aggregates, which then are free to collide (bouncing, merging, or fragmenting), either with other aggregates or free particles. Many survive until coming into contact with another gravitational wake—at which time they are typically destroyed down to their constituent particles, due to the encounter speeds involved. As wakes form on orbital tiamescales, the typical aggregate lifetime is an orbital period as well.

If the wakes are very tightly packed together (e.g., Fig. 2), the lifetime of an aggregate is even shorter, due to the decreased time between annihilating impacts.

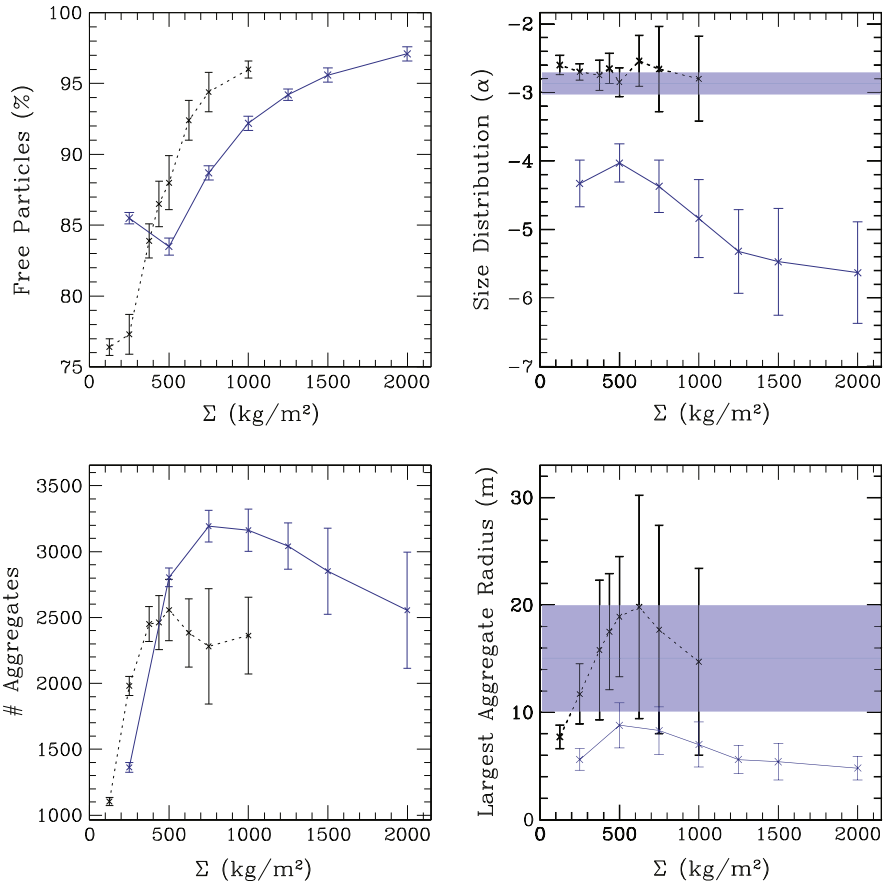

Fig. 5. Four averaged, equilibrated aggregate population properties, calculated as described in Section 2.2, plotted against ring mass surface density (Σ). All points represent separate simulations. The upper-left pane shows the number of unbonded particles in the simulation, as a percentage. The upper-right pane shows the average α, with propagation of error used to combine the errors for each snapshot (from the least-squares fit; see Fig. 3) with the variation of α over time. The lower-left pane shows the number of bonded aggregates (including 2-particle "dumbbells"), and the lower-right shows R_{max}. Suite B-Sig-mono is the solid line (blue), and A-Sig-mono is dotted (black); see Tables 2 and 3. The transparent blue bars on the two right panes show the target observational constraints for both the A and B rings introduced in Section 3.4: $\alpha \sim -2.75$ to -3, and $R_{max} \sim$ 10–20 m. (For interpretation of the references to color in this figure legend, the reader is referred to the web version of this article.)

3.2. Effects of surface density

One of the surprising discoveries of the Cassini era was that the mass surface density (Σ) of the main rings is not as well constrained as previously believed (see Robbins et al., 2010). Consequently, simulations of Saturn's rings should ideally consider a range of Σ values.

Fig. 5 shows our parameter sweep over Σ in both the A and B ring regions. The overall conclusion is that changes in Σ do not change our results with respect to matching observations of α and R_{max} with our data—but there are subtle effects. The number of free particles increases with higher Σ, indicating that higher collision rates tend toward liberation of more free particles rather than trapping more particles into aggregates. The power law index as measured from the simulations is steady in the A ring, with widening errorbars with larger Σ due to higher impact rates (and thus more stochastic aggregate formation). The average R_{max} peaks in the center of our A ring range, but the errorbars are large enough to assume a constant value of 10–20 m.

However, in the B ring, α appears to become steeper with increases in Σ, moving from approximately -4.5 to -5.5. While α appears to saturate at a value of approximately -5.5 at the highest surface densities, additional simulations at high Σ would be required to discover if α stabilizes or continues to fall at ever larger Σ—unfortunately, these simulations are very computationally expensive. On the other hand, R_{max} appears roughly constant with Σ in the B ring, at around 5–10 m.

Thus our A ring results appear insensitive to Σ, but caution is needed when interpreting our B ring results for α, given the large uncertainty in Σ there.

3.3. Dominant fragmentation mechanism: collisions or stress?

Fig. 6 shows the results of our suites studying the response of the aggregate population to variations in the strength parameter, for both the A and B rings. In both regions of the rings, the plots show a sensitivity to the strength below a critical value, and essentially no sensitivity to the strength above that value (to within errorbars). This critical parameter strength, for both the A and B rings, appears to be 10^{-2} Pa (for $\beta = 2$).

Evidently, strength fragmentation is not a significant breakage mechanism above the critical value, as the aggregate populations do not respond to changes in strength above this threshold. For further evidence of this, we point out the A ring simulation with infinite strength (marked at 10^4 Pa on the figure): the results are similar to every simulation at and above the critical strength. That is, above the critical strength, the bonds are essentially infinitely strong, as the typical stresses encountered in these regions of the rings are weaker than the bonds.

In the absence of acceleration-stress fragmentation, the only remaining fragmentation mechanism is impact fragmentation. Thus, when the strength is at or higher than the critical strength, the limiting factor for aggregate size is impact fragmentation,

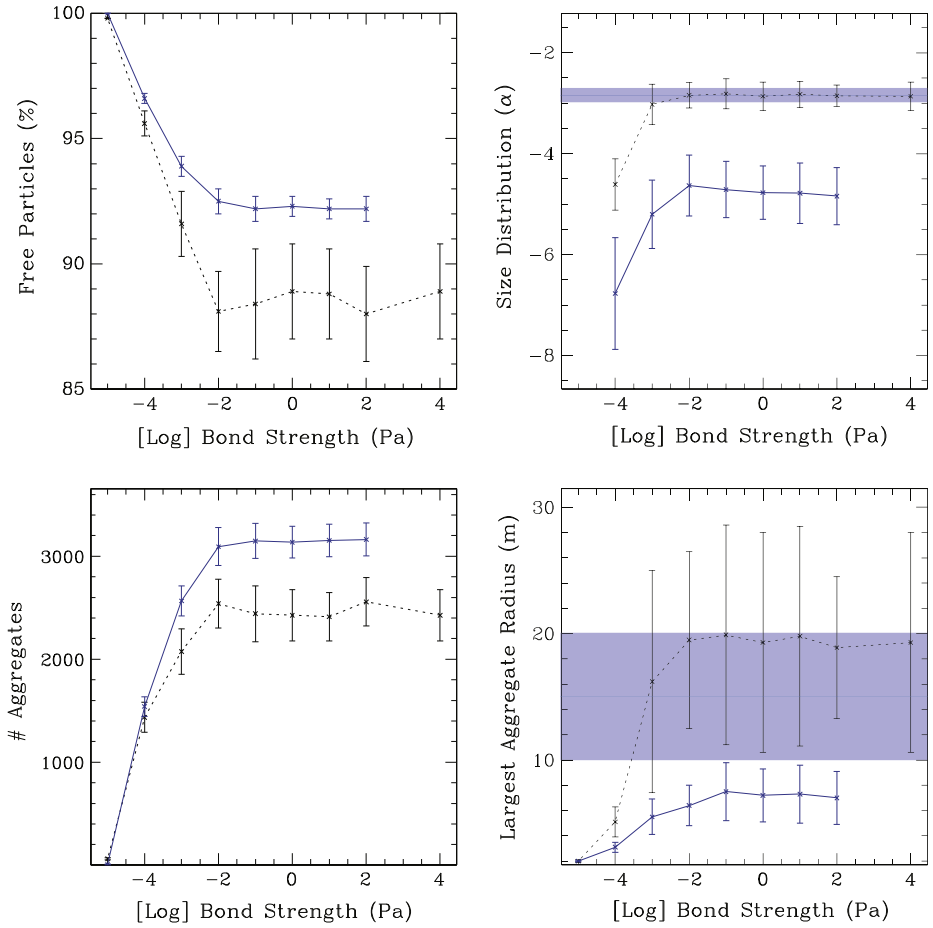

Fig. 6. Four equilibrated aggregate population properties, as described in Fig. 5, plotted against the bond strength (essentially an acceleration threshold for fragmentation). Note that the x-axis is in log space, and that the point plotted at 10^4 Pa represents infinite strength. Lines represent suites B-Str-mono (solid, blue) and A-Str-mono (dotted, black); see Tables 2 and 3. The transparent blue bars on the two right panes show the target observational constraints for both the A and B rings introduced in Section 3.4. (For interpretation of the references to color in this figure legend, the reader is referred to the web version of this article.)

which is governed by the fragmentation limit. If below the critical strength, both stress and impact fragmentation can occur.

The majority of our runs set the fiducial parameter strength to 100 Pa ($\beta = 2$), so those runs are located in the impact-fragmentation-dominated regime. This fiducial is motivated by cometary and laboratory results (see Section 2.1)—but the cometary results are only upper limits, and we are aware that the true strength of these comets may be orders of magnitude below our choice of fiducial strength. However, our fiducial parameter strength is four orders of magnitude larger than our critical value. Thus, even allowing for considerable variation in the strength parameter, real ring particles may still lie in the strength regime that is insensitive to strength fragmentation.[4]

By extension, the discovery of the existence of a critical strength implies that stresses like tidal disruption and aggregate spin are not very important to the discussion of weak cohesive bonding. If bonding is weak enough to allow Saturn's tides to break bonds (parameter strength under 10^{-2} Pa), then, according to the relationship between impact pressure and speed (Eq. (2)), the impact merge and fragmentation limits would be very low: at least 4 orders of magnitude below the merge and fragmentation limits used in this work. These limits would be so low that essentially every collision would be above the fragmentation limit; thus sticking could not occur often, and impacts would rapidly break any bond that does form. Thus, the most important cohesive bonding parameters for the rings are the merge and fragmentation limits. This conclusion assumes that there is a (linear) relationship between impact pressure and speed (that is, that the derivation of Eq. (2) in Paper I is appropriate for Solar System ice).

It should be noted that the value of this critical strength obtained here is dependent on chosen parameters, such as internal particle density, and our range of merge and fragmentation limits. For example, were the aggregates denser (either through higher internal particle density or more efficient packing) they would better resist tidal disruption. Similarly, were our maximum merge and fragmentation limits higher, the aggregates would likely grow to larger sizes—and as they grew, their densities would continue to fall (see Fig. 4). Thus the results here demonstrate the existence of a critical strength in these systems, but the exact value remains dependent on local conditions.

3.4. Constraints on A ring bonding parameters

It was established in Section 3.3 that collisions are the dominant fragmentation mechanism for aggregates in our simulations. Here we examine our results from suites that varied merge and fragmentation limits in order to obtain ranges of those parameters that match observations of the A ring.

We presented some of the observations of α and R_{max} for Saturn's A and B rings in Section 1.1.1, and these results are quite complex. For simplicity, for both the A and B rings, we set our

[4] Note that in this discussion, both the critical and fiducial strengths remain "parameter" strengths, so it is not necessary to translate into "lab" strengths for this comparison. That is, any conversion via β would apply equally to both the fiducial and the critical strengths, canceling out β.

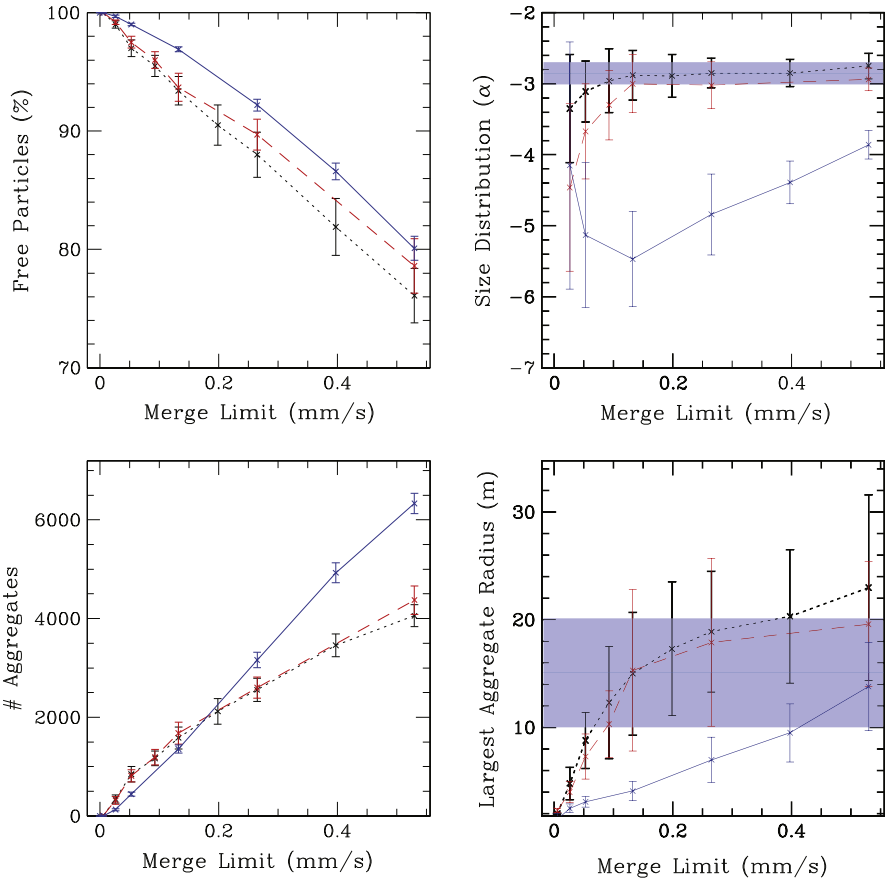

Fig. 7. Four equilibrated aggregate population properties, as described in Fig. 5, plotted against the merge limit, using the lower of our two fiducial fragmentation limits (0.53 mm/s, or $1\,v_{esc}$). All points represent separate simulations with various merge limits. Suite B-M1-mono is the solid line (blue), A-M1-mono is dotted (black), and A-M1-poly is dashed (red); see Tables 1 and 3. The transparent blue bars on the two right panes show the target observational constraints for both the A and B rings introduced in Section 3.4. Note that the property with the most time-variability, and the largest errorbars, is R_{max}. This is a symptom of the stochastic formation of very large bodies that are quickly destroyed, resulting in brief spikes in R_{max} vs. time. (For interpretation of the references to color in this figure legend, the reader is referred to the web version of this article.)

target range for matching the observations of α at -2.75 to -3, and R_{max} at 10–20 m.

We match our chosen criteria for α and R_{max} reasonably well in Fig. 7 at a wide range of merge limits (0.053–0.53 mm/s), using the lower of our two fragmentation limits ($1\,v_{esc}$). Fig. 8, on the other hand, uses the higher fragmentation limit ($2\,v_{esc}$), and only satisfies the criteria for α and R_{max} at one point (0.05 mm/s). Clearly, there is a relationship between fragmentation limit and merge limit: if one value is too extreme, as the fragmentation limit appears to be in Fig. 8, the other parameter's range that matches the observations becomes tiny. Ideally, the best range in one parameter is one that opens the largest matching range in the other. An exhaustive search over plausible combinations of merge and fragmentation limits is possible, but it would require far more simulations than we have performed in this work, so we will simply estimate the bounds on the region of the merge-limit/fragmentation-limit plane that best match the observations.

In Fig. 7 (variable merge limit), the monodisperse data matches the target α and R_{max} values (within error bars) with merge limits of 0.053–0.53 mm/s, while the polydisperse data is slightly more restrictive, with matching merge limits of 0.09–0.53 mm/s. In Fig. 9 (variable fragmentation limit), the A ring line matches the observations for fragmentation limits within 0.4–0.7 mm/s. This result fits with the discussion above, as the constant fragmentation limit in Fig. 8 is outside of the matching range quoted here, causing a limited range of matching merge limits in suite A-M2-mono.

Thus our estimated A ring range for the merge limit is 0.1–0.5 mm/s, and 0.4–0.7 mm/s for the fragmentation limit. We note that the Hatzes et al. (1991) result of a sticking limit at ~0.3 mm/s lies in the center of our range of matching merge limits, lending support to the suggestion that such bonding is possible in the main rings.

3.5. Constraints on B ring bonding parameters

Section 3.4 gave us two sets of constraints that we can now apply to our B ring results: a set of observational criteria, and limits on the bonding parameters that matched our A ring results to those observational constraints.

Applying the observational constraints (target $\alpha = -2.75$ to -3; $R_{max} = 10$–20 m) to the B ring results plotted in Fig. 7 turns up no matching parameters. The data in Fig. 8 is consistent with the observations at merge limits of 0.25–0.4 mm/s (with a fragmentation limit of 1.06 mm/s). Lastly, Fig. 9 satisfies the target α and R_{max} values at fragmentation limits in the 0.9–1.1 mm/s range (with a merge limit of 0.26 mm/s). Evidently, the fragmentation limit of 0.53 mm/s (i.e., $1.0\,v_{esc}$), used for the suite in Fig. 7, was too low to satisfy the B ring observational constraints, which is consistent with that limit being below the matching range found in Fig. 9.

Alternatively, if we assume the bonding parameters are constant throughout the rings, and apply the parameter range that matches our criteria in the A ring (particularly, a fragmentation limit of ~0.5 mm/s) to the B ring data, we find a curious result: α

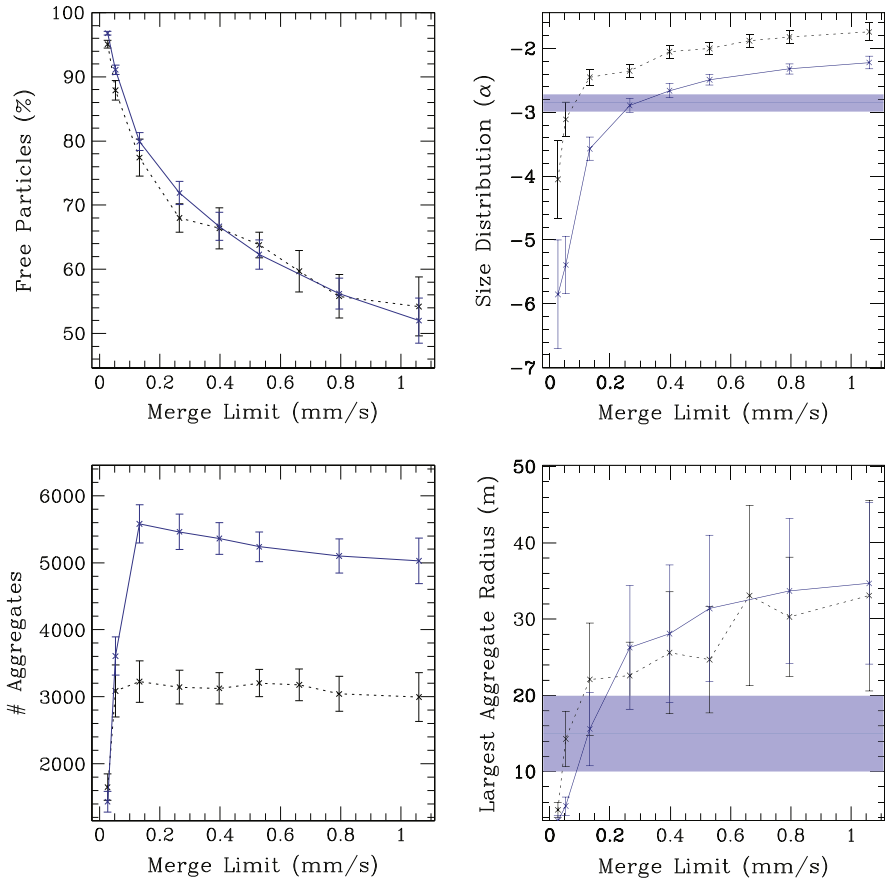

Fig. 8. Four equilibrated aggregate population properties, as described in Fig. 5, plotted against the merge limit, but using the higher of our two fiducial fragmentation limits (1.06 mm/s, or $2v_{esc}$). Suite B-M2-mono is the solid line (blue), and A-M2-mono is dotted (black); see Tables 1 and 3. The transparent blue bars on the two right panes show the target observational constraints for both the A and B rings introduced in Section 3.4. (For interpretation of the references to color in this figure legend, the reader is referred to the web version of this article.)

should be approximately −4 to −5 in the B ring, and R_{max} would be 5–15 m.

What we have discovered is that the observational result of consistent α and R_{max} throughout the rings is at odds with our assumption of constant bonding parameters throughout the rings. We discuss possible resolutions to this conflict in Section 3.6, and devote the rest of this section to discussing why we expect the A and B rings to behave differently in the presence of constant bonding parameters.

We already showed in Section 3.3 that stress fragmentation plays a minor role in these simulations when the strength is above a critical value, and thus collisions dominate the state of the aggregate population, so it cannot simply be that, for example, stronger tides in the B ring give rise to different α and R_{max}. Whatever is causing the B and A ring populations to differ must be collisional in nature. We do not change the properties of the particles themselves (e.g., internal density), so the escape speed (v_{esc}) is the same. It cannot be an effect of Σ, as Fig. 5 shows A and B ring simulations with the same Σ with vastly different results. We believe that it is the slight change in the orbital frequency (Ω), and its resulting change in the shear speed (v_{shear}), that is causing such a drastic difference.

At the semimajor axis of our A ring runs, v_{shear} is 0.37 mm/s (for $R = 1$ m particles), which is well below v_{esc} of 0.53 mm/s (for $R = 1$ m, $\rho = 0.5$ g/cm^3 particles), allowing v_{esc} to dominate the impact speed distribution. But in our B ring runs, Ω is nearly 60% higher than in the A ring, so v_{shear} becomes 0.58 mm/s, which is now slightly larger than the escape speed. Thus the impact speed distribution shifts to larger values in the B ring than the A, as the greater v_{shear} establishes a higher floor of potential encounter speeds. And if impacts tends to be faster in the B ring, the particles will naturally require higher limits—they will need to be "stickier"—if they are to maintain the same equilibrium sizes and size distributions.

This brings up an interesting question: if v_{esc} is constant throughout the disk,[5] but v_{shear} falls with distance from Saturn, at what location in the disk does v_{shear} match v_{esc}—that is, where is the turning point outside of which the escape speed is the dominant impact speed? Both speeds are proportional to the size of the body, so it turns out that their ratio is only dependent on the (assumed constant) internal density of the particles and the distance from Saturn—specifically, $v_{esc}/v_{shear} \sim \sqrt{\rho}/\Omega$. With 0.5 g/cm^3, this location is 106,800 km from Saturn's center,[6] or in the B3 region (Colwell et al., 2009).

If collision-dominated cohesive bonding is occurring in the rings, and particle density is constant (as assumed in this work), we might observe some changes in the particle population's properties around this annulus. Given the parameters found for the A ring, we would predict that α is rather steep (about −4 to −5) in the B ring, with somewhat smaller R_{max} (about 5–10 m in radius).

[5] This is an improper assumption if there are drastic changes in particle properties, such as internal density variations, throughout the disk. Such variations would occur, for example, if the local Roche density is the proper internal density for our indestructible particles. See discussion in Section 3.6.

[6] A $R = 1$ m body with density 0.5 g/cm^3 has $v_{esc} = 0.53$ mm/s. We define $v_{shear} = \frac{3}{2}(2R)\Omega$. Solving for Ω yields 1.8×10^{-4} rad/s, which is at 106,800 km.

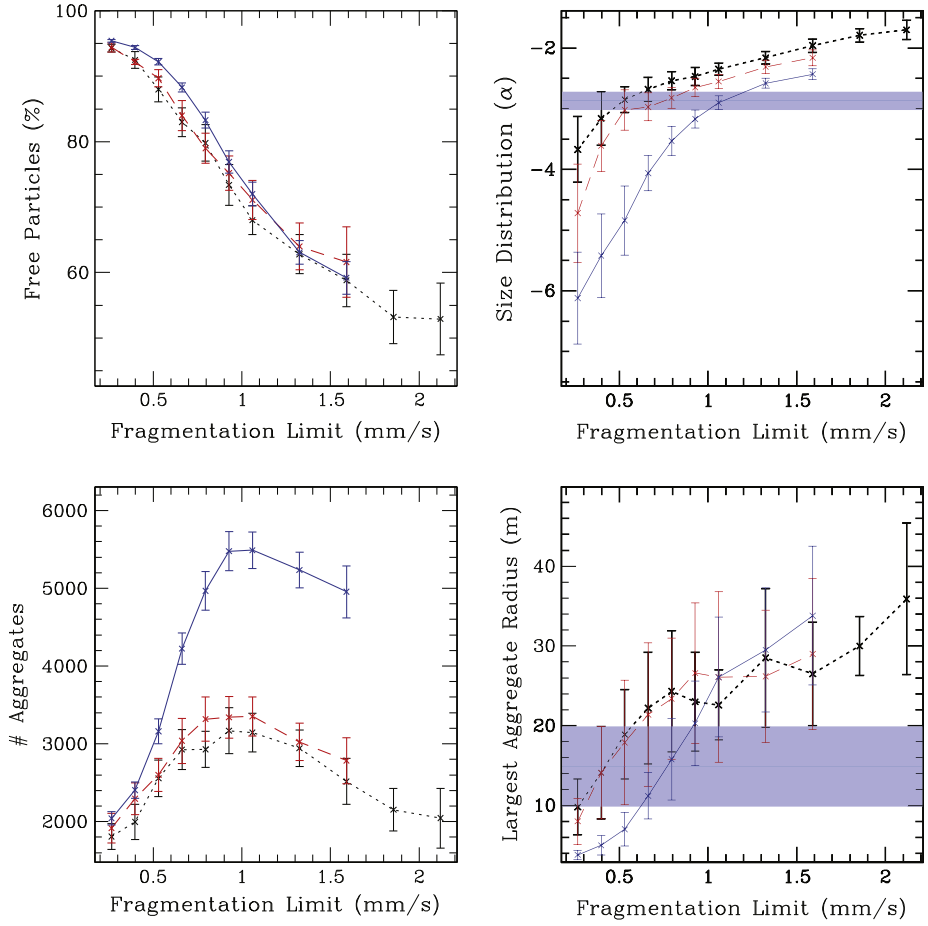

Fig. 9. Four equilibrated aggregate population properties, as described in Fig. 5, plotted against the fragmentation limit, using a fixed merge limit of 0.27 mm/s ($0.5\,v_{esc}$). Suite B-F-mono is the solid line (blue), A-F-mono is dotted (black), and A-F-poly is dashed (red); see Tables 2 and 3. The transparent blue bars on the two right panes show the target observational constraints for both the A and B rings introduced in Section 3.4. (For interpretation of the references to color in this figure legend, the reader is referred to the web version of this article.)

As we move out through the rings, we would expect to see a shallower size distribution (less negative α) with increasing R_{max}, and thus more abundant larger aggregates, as the impacts become milder due to a steady drop in shear speed, with a potentially stronger change around the transition point near the 106,800 km annulus.

It is true that the observations do not seem to agree with our model's predictions for how α should behave, given constant cohesion parameters, but there are hints that perhaps R_{max} is rising with saturnian distance. French and Nicholson (2000) show a constant R_{max} with saturnian distance (20 m), but Voyager observations have hinted otherwise: R_{max} appears to grow from 5 to 10 m in the A ring, and possibly even increases outward through the Cassini division (see Section 1.1.1). While it is encouraging that the observations for R_{max} from Voyager agree loosely with our findings, we acknowledge that it remains far from a satisfying and firm confirmation of our model's results.

3.6. Reconciling observation and model results

In Sections 3.4 and 3.5, we found that we match the observational criteria for bonding in the A ring with a merge limit range of 0.1–0.5 mm/s, and a fragmentation limit range of 0.4–0.7 mm/s. We match those same criteria in the B ring with a merge limit of 0.25–0.4 mm/s, and fragmentation limit of 0.9–1.1 mm/s. These two sets of limits overlap in the merge limit parameter, but—contrary to our assumption of constant cohesion parameters throughout the disk—differ in their range of fragmentation limits by nearly a factor of two.

On the other hand, if we were to apply the A ring's cohesion ranges to the B ring, we would expect steeper size distributions there than in the A ring ($\alpha = -4$ to -5), with smaller largest particles (R_{max} = 5–10 m). Here we provide some discussion on ways to reconcile these differences between prediction and observation.

The first explanation to consider is that these results may indicate that impact-limited weak cohesion is not occurring in the rings—that the observed distribution of particle sizes is simply a result of long-term collisional grinding, with particles never growing and coalescing, but merely fragmenting and shrinking over the age of the Solar System. After all, it is a primary goal of this work to explore whether cohesion is compatible with observations of the rings, and this conflict may show that it is not. However, we have managed to satisfy our observational criteria with reasonable parameters, and may even have begun to explain the observed growth of R_{max} with distance from Saturn. Given these promising findings, we will continue discussing ways to resolve the disagreement.

Next, we consider that the bonding parameters can vary in the main rings, and assume that the size distribution and maximum aggregate size are constant throughout the disk. This implies that the particles in the B ring are "stickier," with a much higher impact fragmentation limit than the particles in the A ring. Given the differences in surface density and orbital frequency between the A and B rings, it is possible that the surface properties of the ring

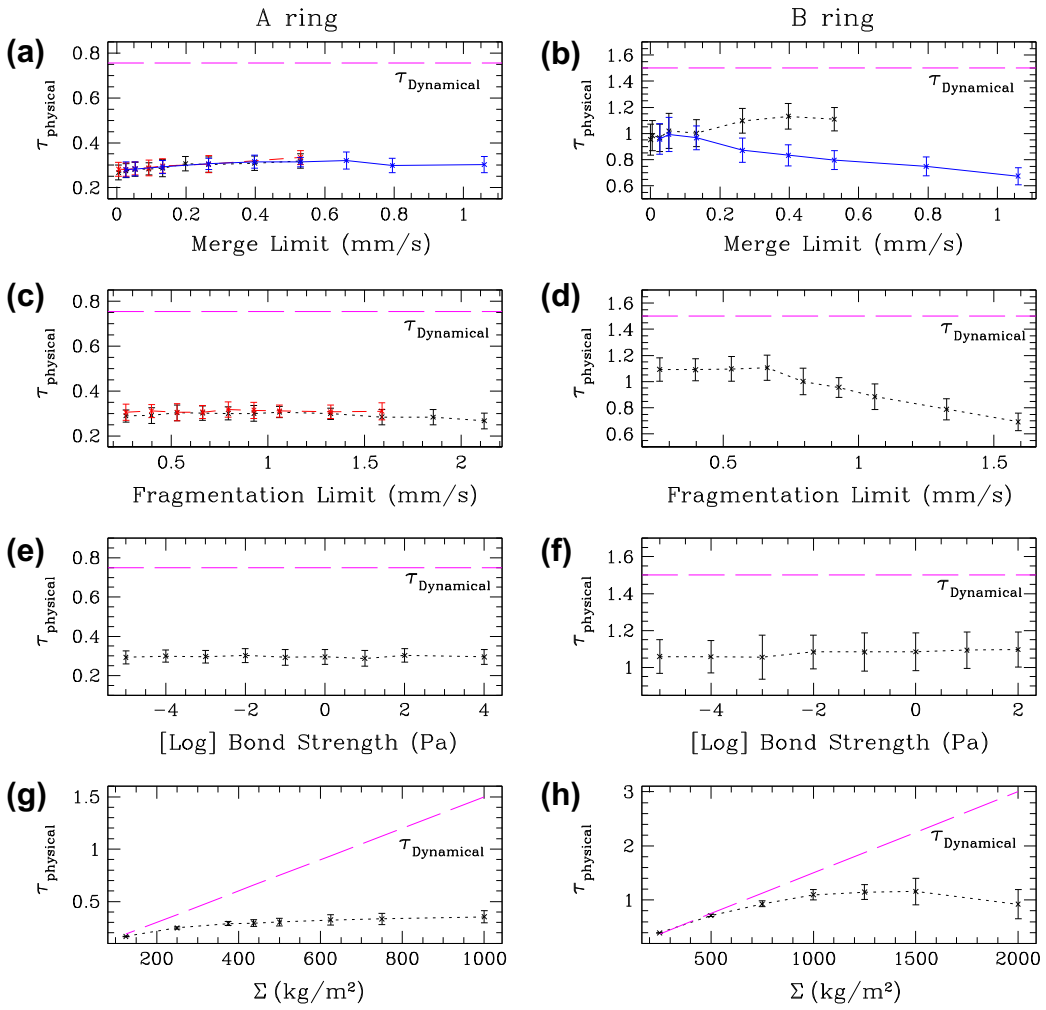

Fig. 10. These eight plots display the equilibrated physical optical depth in all of the simulations in Tables 1–3 using solid (blue), dashed (red) and dotted (black) lines. Each pane also displays the dynamical optical depth (total cross-sectional area of all particles divided by the patch area) for that simulation for comparison, in a long-dashed (magenta) line. Panes on the left are A ring suites (Tables 1 and 2), and those on the right are B ring suites (Table 3). Pane (a) shows suites A-M1-mono in black, A-M2-mono in blue, and A-M1-poly in red; (b) B-M1-mono in black and B-M2-mono in blue; (c) A-F-mono in black and A-F-poly in red; (d) B-F-mono in black; (e) A-Str-mono in black; (f) B-Str-mono in black; (g) A-Sig-mono in black; and finally (h) B-Sig-mono in black. See Section 3.8 for a discussion. Note that the rightmost point in pane (h) refers to an incomplete simulation (see Section 2.1). (For interpretation of the references to color in this figure legend, the reader is referred to the web version of this article.)

particles would be different, and any frost layers on their surfaces would be potentially compacted and refreshed differently due to the higher collision frequency in the B ring. It may be that the bonds formed between cohering particles in the B ring are twice as strong as those in the A ring, but it seems unlikely that these B ring bonds would be exactly as strong as they need to be to match the equilibrium properties of their counterparts in the A ring. Something fundamental would have to link the strength and fragmentation limits of the bonds to the orbital frequency of the particles.

On the other hand, perhaps the cohesion parameters are constant throughout the disk, and α does change with distance from Saturn. This implies that the observations of the B ring measured different structures than our analysis did—and this seems plausible. Figs. 1 and 2 show that the topography of the A and B rings are very different; perhaps the same wavelength of light, interacting with these very different patches of particles, is sensitive to different structures (P. Nicholson, personal communication, 2010). Perhaps more of the wake structure is measured in the B ring than in the A, where individual bodies are more separated. This potential ambiguity in observational measurements is in contrast to the relative simplicity of our measurements within the model; we have the luxury of counting every body separately and measuring its size—regardless of how deeply embedded in a wake it may be. Thus, until we can analyze our real and simulated patches in the same manner, it will be difficult to know exactly how different our results truly are.

We also point out the possibility that a combination of model parameters may exist that provides a constant α with distance from Saturn—under constant cohesion parameters—that our chosen parameter space did not cover. For example, our range of Σ's in the B ring may not truly describe the environment there (e.g., Robbins et al., 2010), so our results may not be accurately modeling the true B ring.

Perhaps more significant is our choice to use a constant internal particle density throughout our simulations, as the value we chose causes our B ring particles to be underdense with respect to the local Roche density there (see Section 2.1). Perhaps growth in our B ring simulations could be enhanced were we to use a higher internal density in those simulations, possibly producing better agreement between our A and B ring results. Specifically, if we were to use the local Roche critical density (ρ_R) for each region of the rings, the ratio of the particle escape speed (v_{esc}) to the local shear speed (v_{shear}) would be constant[7]:

[7] The authors are indebted to Dr. M.S. Tiscareno for pointing this out.

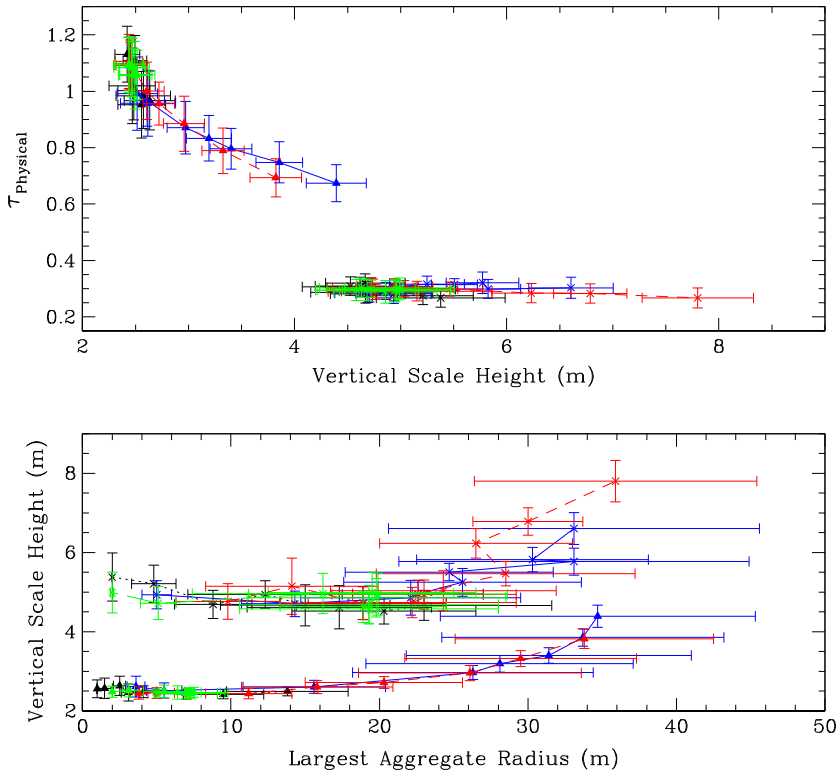

Fig. 11. Composite plot displaying physical optical depth (τ_{phys}) vs. equilibrated vertical scale height (h) in the top pane, and h vs. the radius of the largest aggregate (R_{max}) in the bottom pane, for many of our simulation suites. Symbols distinguish A ring from B ring suites, with triangles for B ring, and $\times$'s for A ring. Colors distinguish which parameter was varied: merge limit suites with a lower fragmentation limit ($1v_{esc}$) are dotted (black), merge limit suites with a higher fragmentation limit ($2v_{esc}$) are solid (blue), fragmentation limit suites are dashed (red), and bond strength suites are long-dashed (green). See Section 3.8 for a discussion. (For interpretation of the references to color in this figure legend, the reader is referred to the web version of this article.)

$$v_{esc}/v_{shear} \sim \sqrt{\rho_R}/\Omega \sim a^{-3/2}/\Omega \sim 1 \quad (3)$$

using $\rho_R \sim 1.88 M_S/a^3$, with M_S, a, and Ω the mass of Saturn, the ring's semimajor axis, and the ring's orbital frequency, respectively. In Section 3.5, we discussed that the differences we observe between our A and B ring simulations are due to the changing value of this ratio—thus if this ratio ought to be constant, these differences may be mitigated.

However, it may not in fact be proper to use the local Roche critical density for the internal density of our indestructible particles in these simulations. The critical Roche density is based on the assumption that the ring material is only held together via self-gravity (no cohesion), and that a body will continue to accrete fluffy icy material, lowering its density, until it fills its gravitational Roche lobe. But this process would itself be enhanced if cohesion is occurring in the rings, causing the particles themselves to potentially overfill their Roche lobes, as the coherent material can grow via cohesive forces as well as gravity. (We know this is happening to the aggregates in our simulations—some possess estimated densities far below the critical density; see Fig. 4.) In this light, perhaps it is not appropriate to assume that ρ_R is the only viable density, but that a range of internal particle densities (including ρ_R) may be plausible. Unfortunately, exploring different material densities was beyond the scope of this study, so such trials are left to future work.[8]

[8] One possible solution (though computationally impractical at this time) would be to use a monodisperse population of very small particles (~1–10 mm) with densities at or near 1 g/cm^3, rather than larger (~1 m) bodies with an assumed porosity, and allow them to accrete to whatever density is natural for the local conditions under study. This may provide more definitive results, but unfortunately the number of particles required is prohibitive (as the number of monodisperse particles increases with the inverse cube of the particle size).

Finally, we must acknowledge that our model remains a first-order attempt at simulating cohesion in planetary rings, and that perhaps our code is too simple, and is missing key physics. While we do not believe our results would change much were we to use a more sophisticated model, the possibility exists.

In summary, we have made a number of suggestions to help reconcile the observational results with our model. In order from least likely to have a significant effect, to most likely to have a large effect, they include: this model may not include key physics that could result in better agreement with observations; cohesion might not be active in the rings (and the observed size distribution arises via another process); particle cohesion parameters vary throughout the rings, which tells us something regarding the (potentially varying) surface properties of the particles; our parameter space was insufficient to fully study this topic; and cohesion parameters are constant throughout the rings, indicating that the ring observations and our data analysis differ in what they are sensitive to.

3.7. Maximum aggregate size in equilibrium

In this section we discuss the largest average aggregate radii (R_{max}) in our equilibrated ring patches, and address how these findings may apply to "propellers" in the A ring, and the suggestion by Tremaine (2003) that large bonded aggregates may exist in the B ring.

We have observed that it is the impact fragmentation limit that appears to determine R_{max} in a simulation. First, we discussed in Section 3.3 that in our simulations, at our chosen parameters, aggregate fragmentation is dominated by collisional fragmenta-

tion, with stress fragmentation playing a minor role in the state of the final aggregate equilibrium population. Then in Figs. 7 and 8, as each portray suites that use constant fragmentation limits, each suite shows evidence for saturation in R_{max} at higher merge limits. On the other hand, Fig. 9 shows consistent growth in R_{max}, with no evident saturation. Thus a rise in fragmentation limit allows R_{max} to rise as well.

As a consequence, we do not expect weak cohesion among ring particles to result in runaway growth: larger aggregates induce faster impacts, as they have higher escape and shear speeds (each of which are proportional to the size of the body—cf. Section 1.2), and so growth will be self-limiting—so long as the fragmentation limit of a body does not increase with the size of a body (or another mechanism does not come into play at larger sizes to strengthen the body). However, it does not seem likely that icy bodies in the rings should grow stronger with size, as larger (terrestrial) rocky bodies tend to be weaker than smaller bodies (e.g., Housen and Holsapple, 1999). If this result applies to ice, the results for R_{max} from our simulations would in fact be too high, as our model makes the simple assumption that the fragmentation limit of a body is constant with size.

The largest aggregates created in our parameter space are approximately 40 m in radius, for both the A and B rings, and only form in simulations that employ the largest fragmentation limits in our parameter space. It is likely that larger aggregates could be made if we extended our parameter range to higher fragmentation limits—but ever higher fragmentation limits lead to stronger disagreement with observations of α, so we do not feel it would be illuminating to provide those models. It is also possible that larger aggregates could be produced if our aggregates had higher overall densities—achieved either though the use of higher internal densities for our indestructible particles (see Section 3.6 for a discussion regarding the local Roche critical density) or by altering our model to allow for compaction of aggregates after they are formed (see Perrine, 2011). Each of these are potential areas of future work—the former being a natural extension of the work presented here (as it is merely exploring further the relevant parameter space), while the latter could require significant model revisions.

Cohesion provides a potential means of constructing large, embedded objects in the dense rings; this is relevant to the discovery of propeller-shaped features in Saturn's outer A ring, as these features appear to be the perturbed wakes of large (yet unresolved) bodies ~20–250 m in radius embedded in the rings. The propellers often manifest in multiple images over time, implying that these perturbations are not simply transient fluctuations in the ring material, and most appear to be confined to three distinct annuli in the A ring (Tiscareno et al., 2008). It is unknown whether these bodies are the remnants of a parent body breakup into three well-defined annuli, whether some mechanism has shepherded these bodies into this configuration (or has preserved them there), or whether they are simply uniquely visible in the observed locations (cf. Tiscareno et al., 2008). Our work explores an alternative, that these propeller bodies are in fact built "bottom-up" out of ring material, rather than "top-down," as the remnants of a larger body.

Our work implies that we can rule out that these bodies are weakly coherent aggregates for three reasons. First, by matching the plausible range of fragmentation limits to observations of α in the A ring, we have confined the range of possible R_{max} values as well, to approximately 15–40 m. In order to create 250 m bodies, we would need much larger fragmentation limits, which would result in α values less negative than -2. Second, these propeller bodies must be long-lived in order to sustain such perturbations over orbital times, and the aggregates in our simulations are created and destroyed on orbital timescales.[9] Third, our model provides no reason why only three distinct annuli of the A ring would produce propeller bodies. On the contrary, if our model is correct, we would expect to see propellers throughout the A ring, with increasingly larger propellers at larger orbital radii, since R_{max} should increase (according to our model) in that sense (assuming constant bonding parameters throughout the rings). It is possible that there is some threshold size that must be reached before a propeller is created (as suggested by simulations in Lewis and Stewart, 2008), yet our model provides no reason for these objects to congregate into distinct regions, rather than distributing themselves evenly throughout the ring. However, we should remind the reader of the caveat presented above regarding aggregate densities: greater internal particle density, or dynamic aggregate compaction (to reduce porosity in an aggregate after it has formed) could allow an aggregate to grow larger by keeping its size below its Hill radius. On the other hand, as indicated in Section 3.3, stress fragmentation plays a lesser role in these simulations than collisional fragmentation (above a critical strength), implying that gravitationally based arguments such as this may not have a great effect (above the critical strength). Of course, these processes are inter-dependent; for example, lowering the size of a body relative to its Hill sphere may lower the critical strength, allowing for collisional fragmentation to dominate at even lower material strengths than presented here. Future work should test the importance of these factors in the growth of aggregates.

Turning our attention to the B ring: Tremaine (2003) suggests that certain large-scale regions of alternating high and low optical depth in the B ring, ~100 km in radial extent, are the result of "shear-free" assemblies of particles—that is, regions of the ring that seem to orbit as a solid body. The present work provides evidence against the suggestion that weak cohesion could build these large structures out of the ring material; while we were able to produce a mix of aggregates, our aggregates' maximum size is limited by the fragmentation limits permitted by our observational constraints, as discussed above. Tremaine (2003) suggests a plausible strength limit (10^4 Pa) which—were the ice that strong—would allow assemblies of such a size to exist. However, our work shows that the impact fragmentation process dominates in regards to the size and lifetime of these objects, and that due to the steady increases in v_{shear} and v_{esc} that occur as these bodies grow, coupled with the scale of v_{shear} in the B ring, impacts should prevent these objects from growing beyond the scale of tens of meters in the B ring. Yet, similar to the previous paragraph, this conclusion is subject to the findings of future work. For example, different choices for the internal particle density between the A and B ring simulations should change the relationship between v_{shear} and v_{esc}, likely altering the findings presented here—as discussed in Sections 3.5 and 3.6.

3.8. Other observational diagnostics for constraining aggregation parameters

To this point, we have focused on constraining bonding parameters to match existing observations of the A and B rings of Saturn (specifically, α and R_{max}). We will now discuss the effects of cohesion parameters on two other potentially observable properties of the rings: the physical optical depth (τ_{phys}) and the scale height (h). If we can show these properties vary with "stickiness," perhaps we can do more than simply constrain the plausible parameter range.

Fig. 10 shows the equilibrated τ_{phys} for each of the simulations in Tables 1–3. We first point out that the bottom pane of Fig. 10

[9] While it remains possible that larger aggregates may have longer lifetimes due to self-shielding effects, we argue that increases in velocity dispersion from gravitational stirring, and increased shear speed, would destroy these massive bodies just as quickly as the smaller aggregates.

shows nearly constant τ_{phys} for most Σ values in the A and B ring. This agrees with the findings of Robbins et al. (2010), who discussed the nonlinear relationship between optical depth and Σ by providing simulations that showed that one cannot assume that rises in Σ will produce a corresponding linear rise in τ_{phys} (especially at large τ). Thus the following discussion should hold no matter the value of the local surface density (cf. Section 3.2).

It appears from these results that τ_{phys} in the A ring is not sensitive to changes in any cohesion parameter—which unfortunately means that τ_{phys} may not be a useful diagnostic for cohesion in the A ring. However, in the B ring, τ_{phys} can vary with cohesion parameter by as much as 30%, from $\tau_{phys} \sim 1$ with no cohesion, to $\tau_{phys} \sim 0.7$ at very high merge or fragmentation limits. So, for example, if cohesion parameters were to vary greatly in the B ring, we might be able to observe a change in τ_{phys}.

But why do the same parameters cause changes to τ_{phys} in the B ring, but no changes in the A ring? The answer appears to lie in the scale height of those two regions of the rings. Tests we have performed revealed a nearly-linear relationship between patch semimajor axis and scale height, even in the absence of any cohesion. (A similar increase in scale height with orbital distance was noted previously by Salo (1995); see Fig. 14 in that work.) Geometrically, if the material in the A ring is more vertically distributed, there is a greater chance for particles to move above or below one another, reducing the physical optical depth. Thus, even at the same surface densities, an A ring simulation ought to have a lower equilibrium τ_{phys} than an equivalent B ring simulation (which is what we find).

The top pane of Fig. 11 shows that h is consistently higher in the A ring simulations, while τ_{phys} is always lower in the A ring. In fact, h appears to be so high in the A ring that changes to h do not affect the optical depth (this is presumably because h remains large enough to allow particles to consistently move above or below one another). Conversely, points generally in the upper-left corner of the top pane (B ring data, with weaker cohesion) have low h, and thus such a compact configuration of particles ($h \sim 2$–3 m) that any increase in h (with stronger cohesion parameters) has a significant effect on τ_{phys} in the B ring.

Why does h increase with stronger cohesion? In the bottom pane of Fig. 11, we see that h is excited by increases in the size of the largest aggregate (R_{max}). The scale height appears nearly constant[10] with changes in R_{max} until ~20–25 m, when increases in R_{max} cause h to grow at the highest cohesion parameters (see Figs. 7–9 to map the cohesion parameters to R_{max}).

Thus when cohesion is strong enough to produce aggregates larger than ~20–25 m, the particle population responds to the gravitational excitations of these bodies and becomes vertically excited, causing h to rise. If this disk is already several particles thick, as in the A ring, the optical depth does not fall; but if the rings are ordinarily compact, then this rise in h will cause a decrease in τ_{phys}.

Our observational criteria included the assumption that aggregates do not grow larger than ~20 m in the B ring, and we find that τ_{phys} would only change if aggregates could grow to this size or larger. Thus searching for variations in τ in order to constrain potential cohesion parameters would also potentially shed light on the size of the largest aggregate in the rings.[11]

[10] We note that in the A ring suites, h decreases slightly with increasing R_{max} until ~8 m. We speculate that perhaps cohesion is providing a damping effect (via collisions with zero coefficient of restitution) at these weakly cohesive parameters—an effect that is overtaken at higher cohesion values when the gravitational influence of the large aggregates re-excites the disk.

[11] It would be more direct to observe local variations in h to constrain R_{max}; however such a study would require sub-meter resolution on the vertical structure of the main rings, which is far beyond the capabilities of past or present space missions.

3.9. Validity of monodisperse starting conditions

To support the analysis above, we examine a major simplification in the model and determine if it is acceptable—namely, that the use of a monodisperse population of particles (with a uniform 1 m radius) matches the results of the polydisperse comparison cases (radii 0.8–1.2 m, $\alpha = -3$). We ran two comparison suites with polydisperse particles, A-M1-poly and A-F-poly, and their results are plotted with A-M1-mono and A-F-mono in Figs. 7 and 9, respectively.

To first order, the results show good agreement, as the points often lie within each other's errorbars. But closer inspection shows that where differences are visible, the polydisperse results are systematically offset from the monodisperse data, with the polydisperse runs having fewer aggregated particles, smaller largest aggregates (R_{max}), steeper size distributions, and more (smaller) aggregates overall. It is possible that the presence of the more massive indestructible particles in the polydisperse cases (up to 1.2 m) is increasing the velocity dispersion in those runs, leading to subtle differences between the cases. Close examination of the average velocity dispersion in these simulations, comparing monodisperse to polydisperse runs, is mostly inconclusive, as the errorbars overlap. However, at higher merge limits, the polydisperse runs indeed show higher velocity dispersions.

Excited to higher velocity dispersions, the polydisperse particles are subject to higher-speed impacts, leading to fewer merging events, and more fragmentation events. This would naturally cause the observed systematic effects.

We note that this is likely an artificial difference: if these 1.2 m particles were able to fragment, they would not likely have the same enduring effect on the velocity dispersion. This could be tested using a polydisperse population with a smaller maximum size—however, using smaller particles causes a rapid rise in the number of particles (for a simulated region of a fixed size and surface density), and we have not attempted such runs at this time.

It would appear that our polydisperse and monodisperse cases provide similar results, and that our results would not differ significantly were we to use a polydisperse initial size distribution throughout our runs. This conclusion would be stronger if we were able to compare to a wider range of polydisperse particles (e.g., 0.1–1 m), but this was unfortunately not computationally practical with the number of simulations required. Future work should push the these limits and continue to test the validity of the monodisperse case.

3.10. Comments on our range of bonding parameters

Our chosen range of cohesion model parameters (merge and fragmentation limits, and bond strength) appears to cover the most significant and interesting regions of the parameter space that affect the equilibrium aggregate population. In many of the panes in Figs. 6–9, the data show signs of saturation.

At small strengths, and merge and fragmentation limits, we approach 0% bonding. At higher merge and fragmentation limits, we begin to see evidence for saturation in the percentage of bonded particles, as well as α, and R_{max}. This is almost certainly the result of our chosen parameter range bracketing the common impact speeds of the rings (the particles' escape speeds and the shear speed of the regions of the rings we modeled). We predict that our figures would look quite different if the impact speed distribution were centered around other values—that is, if the velocity dispersions of our particles were different. So any alternative choice of parameters that could affect the equilibrium velocity dispersion (e.g., the coefficient of restitution) might in turn affect the equilibrium aggregate population.

We also note that our bond strength range is large enough to encompass both the critical strength value (see Section 3.3) and infinite strength (in one A ring simulation).

We believe that we have sampled the most significant portions of the parameter space that are relevant to the A and B rings of Saturn; however, we note that cohesion should produce different results in other systems with vastly different velocity dispersions, such as protoplanetary disks in the process of forming planets—requiring a different range of parameters not likely covered by this work.

4. Summary and conclusions

We have used our new local *N*-body code, presented in Paper I, to explore the possibility that cohesion, via the sticking process studied by Hatzes et al. (1991), might be occurring in the A and B rings of Saturn.

We find that cohesion is consistent with observations ($\alpha = -2.75$ to -3; $R_{max} = 10$–20 m) in both the A ring and B rings. We can constrain the merge limit in the A ring to 0.1–0.5 mm/s, which brackets the Hatzes et al. (1991) result that frosty ice sticks at impact speeds below 0.3 mm/s. We can constrain the fragmentation limit in the A ring to 0.4–0.7 mm/s, which has no experimental reference.

The same observational criteria constrain the merge limit in the B ring to 0.25–0.4 mm/s, and the fragmentation limit to 0.9–1.1 mm/s. If we instead apply the cohesion parameters found for the A ring to the B ring, we find steeper size distributions ($\alpha \sim -5$ to -4) and smaller largest bodies ($R_{max} \sim 5$–10 m).

We discussed possible conclusions we could draw from these separate constraints in Section 3.6. For instance, it could be that aggregates in the B ring somehow have stronger cohesive bonds through differences in the particles' surface texture there. Or perhaps the observations of the rings we are using as criteria are sensitive to different structures than our analysis is, and the size distribution of particles in the B ring truly is steeper than has been reported by observations.

We find a critical parameter strength in both rings of 10^{-2} Pa (i.e., $\beta = 2$), above which collisions dominate the state of the aggregate population, and stresses like tidal disruption and spin are negligible. For the sticking model presented in Hatzes et al. (1991), we estimate $\beta = 10^{-3}$, making the critical laboratory strength 10 Pa for that cohesion model. This value is lower than lab strengths measured for icy frost by experiments (e.g., ~100 Pa; Supulver et al., 1997), and is consistent with (or lower than) the upper limits for cometary results (~5 Pa for SL9, ~100 Pa for Brooks 2, and $\sim 10^3$–10^4 for Temple 1; see Section 2.1). Thus it is possible that ice in the rings, were it to form into frosty aggregates, could plausibly be as strong as (or stronger than) the critical strength we have found.

Applying both the discovery of a plausible critical strength and our simple scaling relationship between impact pressure and speed (see Section 2.1), we conclude that at these material densities, tides and reasonable aggregate spin rates are not significant fragmentation factors for weakly cohesive aggregates in the rings, and are not the limiting factor in aggregate growth. If the strength is above the critical strength, impact fragmentation is the dominant breakage mechanism. If the strength is lower than the critical strength, then the scaling relationship (Eq. (2)) implies that the fragmentation limit must be so low as to make aggregate survival impossible.

We find that the maximum size of our aggregates is determined by the choice of fragmentation limit (so long as the strength is set above the critical value). As the plausible range of fragmentation limits is restricted by observations of α, the largest bodies this model can produce are approximately 40 m in radius. This could imply that propeller progenitors, as well as Tremaine's (2003) shear-free regions, are not collections of weakly cohesive frosty ice particles. However, further work (particularly to explore the effect of variations in internal particle density) is needed to resolve these questions fully.

It might be possible to provide constraints on cohesion parameters in the B ring by searching for abnormally low physical optical depths, but these variations should only occur at the largest of cohesion parameters that allow the aggregates to grow beyond 20–25 m in radius. It appears that cohesion parameters have no effect on the optical depth in the A ring.

Our overall conclusion is that our results are generally consistent with frosty ice cohesion occurring in the rings—though we fully acknowledge that consistency by no means implies proof. To find proof, the cohesive model could be used to explore other ring phenomena. For instance, one might determine if any relationship exists between the azimuthal brightness asymmetry and cohesion; or investigate the effects of cohesion on ring viscosity (cf. Daisaka and Ida, 1999), as applied to wave damping, or overstability. Finally, true proof should be possible if the rings could be imaged with sub-meter resolution, so that we may directly resolve any aggregates of coherent particles forming in the wakes—but such a mission is not currently planned.

Note that the exact numerical results presented here for the three bonding model parameters (merge limit, fragmentation limit, and parameters strength) are sensitive to our choices for other parameters (e.g., internal particle densities, coefficient of restitution) and data analysis strategy (temporal averaging of snapshots, rather than stacking snapshots into a single size distribution). For example, the quoted range of merge and fragmentation limits that match the target constraints, and the value of the critical strength, would likely change given other choices. However, the overall conclusion of this work—that weak cohesion is a plausible and potentially important mechanism in dense rings—would remain unchanged.

Acknowledgments

R.P.P. acknowledges support from the National Aeronautics and Space Administration under the NASA Earth and Space Science Fellowship program, and the University of Maryland Graduate School's Ann G. Wylie Dissertation Fellowship, D.C.R. from Grant No. NNX08AM39G issued through the Office of Space Science, and R.P.P. and D.C.R. jointly from Grant No. NNX10AQ01G issued through the Office of Space Science. The authors thank Dr. Tiscareno and an anonymous reviewer for their insightful and detailed comments that greatly improved this manuscript.

The simulations presented in this paper were carried out using computing clusters administered by the Center for Theory and Computation of the Department of Astronomy at the University of Maryland ("yorp"), and the Office of Information Technology at the University of Maryland ("deepthought").

Raytracing for Figs. 1 and 2 was performed using the Persistence of Vision Raytracer.[12]

References

Albers, N., Spahn, F., 2006. The influence of particle adhesion on the stability of agglomerates in Saturn's ring. Icarus 181, 292–301.

Asphaug, E., Benz, W., 1996. Size, density, and structure of Comet Shoemaker–Levy 9 inferred from the physics of tidal breakup. Icarus 121, 225–248.

Barnes, J., Hut, P., 1986. A hierarchical O(Nlog$N$) force-calculation algorithm. Nature 324, 446–449.

[12] http://www.povray.org/.

Borderies, N., Goldreich, P., Tremaine, S., 1984. Unsolved problems in planetary ring dynamics. In: Greenberg, R., Brahic, A. (Eds.), Planetary Rings. Univ. of Arizona Press, Tucson, pp. 713–734.
Bridges, F.G., Hatzes, A., Lin, D.N.C., 1984. Structure, stability and evolution of Saturn's rings. Nature 309, 333–335.
Bridges, F.G., Supulver, K.D., Lin, D.N.C., Knight, R., Zafra, M., 1996. Energy loss and sticking mechanisms in particle aggregation in planetesimal formation. Icarus 123, 422–435.
Bridges, F., Supulver, K., Lin, D.N.C., 2001. Energy loss and aggregation processes in low speed collisions of ice particles coated with frosts or methanol/water mixtures. In: Poschel, T., Luding, S. (Eds.), Granular Gases. Springer, Berlin/Heidelberg, pp. 153–183.
Colwell, J.E., Nicholson, P.D., Tiscareno, M.S., Murray, C.D., French, R.G., Marouf, E.A., 2009. The structure of Saturn's rings. In: Dougherty, M.K., Esposito, L.W., Krimigis, S.M. (Eds.), Saturn from Cassini–Huygens. Springer, Dordrecht, pp. 375–412.
Cuzzi, J. et al., 2009. Ring particle composition and size distribution. In: Dougherty, M.K., Esposito, L.W., Krimigis, S.M. (Eds.), Saturn from Cassini–Huygens. Springer, Dordrecht, pp. 459–510.
Daisaka, H., Ida, S., 1999. Spatial structure and coherent motion in dense planetary rings induced by self-gravitational instability. Earth Planets Space 51, 1195–1213.
French, R.G., Nicholson, P.D., 2000. Saturn's rings II: Particle sizes inferred from stellar occultation data. Icarus 145, 502–523.
French, R.G., Salo, H., McGhee, C.A., Dones, L., 2007. HST observations of azimuthal asymmetry in Saturn's rings. Icarus 189, 493–522.
Hatzes, A.P., Bridges, F., Lin, D.C., Sachtjen, S., 1991. Coagulation of particles in Saturn's rings—Measurements of the cohesive force of water frost. Icarus 89, 113–121.
Housen, K.R., Holsapple, K.A., 1999. Scale effects in strength-dominated collisions of rocky asteroids. Icarus 142, 21–33.
Julian, W.H., Toomre, A., 1966. Non-axisymmetric responses of differentially rotating disks of stars. Astrophys. J. 146, 810–827.
Karjalainen, R., 2007. Aggregate impacts in Saturn's rings. Icarus 189, 523–537.
Karjalainen, R., Salo, H., 2004. Gravitational accretion of particles in Saturn's rings. Icarus 172, 328–348.
Lewis, M.C., Stewart, G.R., 2000. Collisional dynamics of perturbed planetary rings. I. Astron. J. 120, 3295–3310.
Lewis, M.C., Stewart, G.R., 2008. Features around embedded moonlets in Saturn's rings: The role of self-gravity and particle size distributions. Icarus 199, 387–412.
Lois, G., Carlson, J.M., 2007. Force networks and the dynamic approach to jamming in sheared granular media. Europhys. Lett. 80, 58001.
Perrine, R.P., 2011. *N*-body Simulations with Cohesion in Dense Planetary Rings. Thesis, University of Maryland, College Park. 137pp.
Perrine, R.P., Richardson, D.C., Scheeres, D.J., 2011. A numerical model of cohesion in planetary rings. Icarus 212, 719–735.
Porco, C.C., Thomas, P.C., Weiss, J.W., Richardson, D.C., 2007. Saturn's small inner satellites: Clues to their origins. Science 318, 1602–1607.
Porco, C.C., Weiss, J.W., Richardson, D.C., Dones, L., Quinn, T., Throop, H., 2008. Simulations of the dynamical and light-scattering behavior of Saturn's rings and the derivation of ring particles and disk properties. Astron. J. 136, 2172–2200.
Richardson, D.C., 1994. Tree code simulations of planetary rings. Mon. Not. R. Astron. Soc. 269, 493–511.
Richardson, D.C., 1995. A self-consistent numerical treatment of fractal aggregate dynamics. Icarus 115, 320–335.
Richardson, D.C., Quinn, T., Stadel, J., Lake, G., 2000. Direct large-scale *N*-body simulations of planetesimal dynamics. Icarus 143, 45–59.
Richardson, D.C., Leinhardt, Z.M., Melosh, H.J., Bottke Jr., W.F., Asphaug, E., 2002. Gravitational aggregates: Evidence and evolution. In: Bottke, W.F., Jr., Cellino, A., Paolicchi, P., Binzel, R.P. (Eds.), Asteroids III. Univ. of Arizona Press, Tucson, pp. 501–515.
Richardson, J.E., Melosh, H.J., Lisse, C.M., Carcich, B., 2007. A ballistics analysis of the Deep Impact ejecta plume: Determining Comet Tempel 1's gravity, mass, and density. Icarus 190, 357–390.
Robbins, S.J., Stewart, G.R., Lewis, M.C., Colwell, J.E., Sremcevic, M., 2010. Estimating the masses of Saturn's A and B rings from high-optical depth *N*-body simulations and stellar occultations. Icarus 206, 431–445.
Salo, H., 1992. Gravitational wakes in Saturn's rings. Icarus 359, 619–621.
Salo, H., 1995. Simulations of dense planetary rings. III. Self-gravitating identical particles. Icarus 117, 287–312.
Salo, H., Karjalainen, R., French, R.G., 2004. Photometric modeling of Saturn's rings. II. Azimuthal asymmetry in reflected and transmitted light. Icarus 170, 70–90.
Schmidt, J., Ohtsuki, K., Rappaport, N., Salo, H., Spahn, F., 2009. Dynamics of Saturn's dense rings. In: Dougherty, M.K., Esposito, L.W., Krimigis, S.M. (Eds.), Saturn from Cassini–Huygens. Springer, Dordrecht, pp. 413–458.
Sekanina, Z., Yeomans, D.K., 1985. Orbital Motion, nucleus precession, and splitting of periodic Comet Brooks 2. Astron. J. 90, 2335–2352.
Sitko, M.L. et al., 2011. Infrared spectroscopy of Comet 73P/Schwassmann–Wachmann 3 using the Spitzer Space Telescope. Astron. J. 142, 80.
Spahn, F., Albers, N., Sremcevic, M., Thornton, C., 2004. Kinetic description of coagulation and fragmentation in dilute granular particle ensembles. Europhys. Lett. 67, 545–551.
Stadel, J., 2001. Cosmological *N*-body Simulations and their Analysis. Thesis, University of Washington, Seattle. 126pp.
Supulver, K.D., Bridges, F.G., Lin, D.N.C., 1995. The coefficient of restitution of ice particles in glancing collisions: Experimental results for unfrosted surfaces. Icarus 113, 188–199.
Supulver, K.D., Bridges, F.G., Tiscareno, S., Lievore, J., Lin, D.N.C., 1997. The sticking properties of water frost produced under various ambient conditions. Icarus 129, 539–554.
Tiscareno, M.S., Burns, J.A., Nicholson, P.D., Hedman, M.M., Porco, C.C., 2007. Cassini imaging of Saturn's rings II. A wavelet technique for analysis of density waves and other radial structure in the rings. Icarus 189, 14–34.
Tiscareno, M.S., Burns, J.A., Hedman, M.M., Porco, C.C., 2008. The population of propellers in Saturn's A ring. Astron. J. 135, 1083–1091.
Toomre, A., 1964. On the gravitational stability of a disk of stars. Astrophys. J. 139, 1217–1238.
Tremaine, S., 2003. On the origin of irregular structure in Saturn's rings. Astron. J. 125, 894–901.
Wisdom, J., Tremaine, S., 1988. Local simulations of planetary rings. Astron. J. 95, 925–940.
Zebker, H.A., Marouf, E.A., Tyler, G.L., 1985. Saturn's rings: Particle size distributions for thin layer model. Icarus 64, 531–548.